CRYSTAL GROWTH & DESIGN

pubs.acs.org/crystal

Article



# Identifying Structure and Texture of Metal−Organic Framework $Cu_2(bdc)_2(dabco)$ Thin Films by Combining X-ray Diffraction and Quantum Mechanical Modeling

Mario Fratschko, Nina Strasser, Narges Taghizade, Mercedes Linares-Moreau, Jan C. Fischer, Tonghan Zhao, Ian A. Howard, Paolo Falcaro, Egbert Zojer,* and Roland Resel*

Cite This: *Cryst. Growth Des.* 2025, 25, 3665−3679

Read Online

ACCESS | Metrics & More | Article Recommendations | Supporting Information

**ABSTRACT:** This study describes a strategy for unambiguously determining metal−organic framework (MOF) thin film structures, which is demonstrated for a pillar-layer MOF consisting of Cu paddlewheel nodes connected by benzene-1,4-dicarboxylate (bdc) linkers and 1,4-diazabicyclo[2.2.2]octane (dabco) pillars. An initial structural model is derived by isostructural replacement from the material's $Zn^{2+}$ analogue. This is followed by a structure optimization using density functional theory. The model is supported by comparing calculated and measured diffraction patterns and infrared spectra for two differently grown thin films. Key to verifying the structure and identifying the thin film texture are grazing incidence X-ray diffraction (GIXD) experiments with rotating samples. These probe the majority of reciprocal space and thus also allow a straightforward generation of pole figures for various diffraction peaks. Two types of films are prepared either by layer-by-layer deposition or by ceramic-to-MOF conversion. Both share the same phase but display clearly different textures: a uniplanar texture in the case of the layer-by-layer grown film and a distorted axial texture with an epitaxial alignment between MOF and $Cu(OH)_2$ crystallites for the ceramic-to-MOF-converted film. The variations in the texture follow from differences in the substrate surfaces. Our findings highlight the potential of performing GIXD experiments on rotating samples (augmented by theoretical modeling) to (i) determine the texture of MOF thin films and (ii) to solve MOF crystal structures from thin film data even for strongly varying textures.

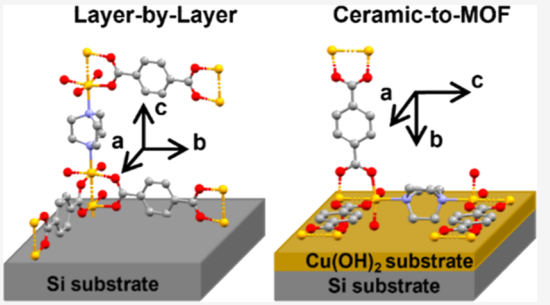




## 1. INTRODUCTION

Metal−organic frameworks (MOFs) are extended materials formed by an internal network of metal ions or clusters connected by organic ligands.[1] They are typically crystalline with high surface areas, tunable pores, and good thermal and chemical stability.[2] These properties make them ideal for gas storage and separation,[3−6] drug delivery,[7−10] sensing[11−13] and catalysis.[14−16] The synthesis of MOFs is extremely versatile and can be accomplished by combining metal ions and organic ligands under a variety of conditions, including hydrothermal and solvothermal synthesis, microwave synthesis, or electrochemical and mechanochemical treatments.[17−20] Usually, MOF crystals with different sizes from tens of nanometers up to millimeters are produced. However, for various applications, such as electronic devices, thin films are required.[21−24] In order to improve the performance of MOF thin films for different applications, controlling the texture (i.e., orientation) of the crystallites is highly desirable.[25−27] For example, a defined alignment of the pores can enable enhanced transport of molecules or electrical charge through MOFs, and it can also trigger the alignment of guest-molecules.[28−30] Oriented MOF thin films are typically fabricated using dedicated techniques, such as gas phase,[31,32] layer-by-layer (LbL),[27] or heteroepitaxial[25,30] growth, among others.

In order to optimize and understand the processes of thin film formation, it is necessary to conduct a detailed crystallographic characterization of the grown films. In this context, X-ray diffraction is the method of choice for obtaining a basic understanding of the type of phase, the preferred orientation of the crystallites relative to the substrate surface, and the epitaxial alignment.[33] In particular, for thin film characterization, grazing incidence X-ray diffraction (GIXD) is the most suitable technique.[34−36] Various strategies can be applied to analyze the data, including phase analysis by comparing experimental and calculated peak patterns[37] or a detailed analysis of peak positions and peak intensities to determine the crystallographic lattices and the arrangement of the metal atoms and linkers

Received: October 17, 2024
Revised: April 25, 2025
Accepted: April 28, 2025
Published: May 19, 2025

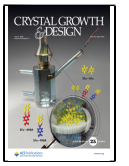

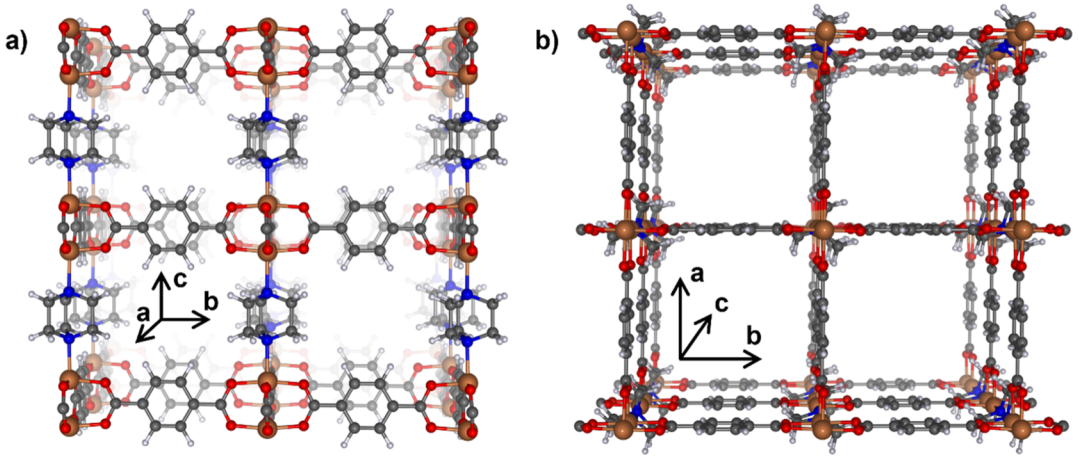


**Figure 1.** 3D-view of $Zn_2(bdc)_2(dabco)$ framework structure along (a) the *a*-direction and (b) along the *c*-direction. 2D sheets formed by benzene-1,4-dicaboxylate (bdc) are connected by 1,4-diazabicyclo[2.2.2]octane (dabco). Zn brown; N blue; O red; C gray; and H white.

within the unit cell.[38] Of particular interest in this context are GIXD experiments in which the sample is rotated during the measurements (rotating-GIXD) so that a significant fraction of reciprocal space is probed. This provides a much more in-depth knowledge of the actual structure of the studied thin films compared to, e.g., single in-plane and out-of-plane diffraction experiments or GIXD measurements at fixed sample orientations. Still, the latter two techniques are commonly applied for studying MOF thin films due to their faster and easier measurement process, despite the limited amount of data they provide compared with rotating-GIXD experiments. In fact, when combining in-plane and out-of-plane diffraction experiments, one probes only a tiny fraction of reciprocal space. Moreover, the data from GIXD experiments at fixed sample rotation are comprehensive only if one can safely assume a uniplanar texture or randomly oriented crystallites.

Rotating the sample during GIXD measurement besides a more comprehensive structural characterization also allows the extraction of pole figures.[39] These provide direct information on the distribution of the orientations of crystallites (i.e., the crystallographic texture). They also reveal possible epitactic relationships between substrates and the thin films.[39] Still, to date they have rarely been used for investigating MOF thin films.[38,40,41]

As a reference system for portraying the potential of the rotating-GIXD approach augmented with quantum-mechanical modeling, we chose $Cu_2(bdc)_2(dabco)$. The motivation for this choice is 2-fold: (i) the crystal structure of $Cu_2(bdc)_2(dabco)$ has not been explicitly solved so far and (ii) $Cu_2(bdc)_2(dabco)$ thin films can be grown with fundamentally different textures depending on the used growth method. Both aspects provide a comparably straightforward way of presenting the potential of the proposed combined theoretical and experimental approach.

In fact, $Cu_2(bdc)_2(dabco)$ has been suggested to have an $M_2L_2P$ structure[42] (M: metal ion, L: layer linker, and P: pillar linker). This is based on the assumption that $Cu_2(bdc)_2(dabco)$ is isostructural to $Zn_2(bdc)_2(dabco)$, whose paddlewheel complexes are connected by benzene-1,4-dicarboxylate (bdc) linkers forming 2D layers. These layers are then connected by (dabco) units.[43,44] This results in a 3D network. The $Zn_2(bdc)_2(dabco)$ framework structure is sketched in Figure 1. In its powder form, $Cu_2(bdc)_2(dabco)$ MOF was prepared already about 20 years ago by Seki et al.[43,45] From a practical point of view, $Cu_2(bdc)_2(dabco)$ is interesting due to its high surface area exceeding 700 $m^2/g$. Thus, it, for example, has a high potential in gas adsorption and storage.[25,45−47]

For the present study, we focus on the crystallographic characterization of $Cu_2(bdc)_2(dabco)$ thin film samples prepared by two complementary methods: (1) LbL growth on silicon[48] and (2) heteroepitaxial growth by ceramic-to-MOF (CtM) conversion of highly aligned $Cu(OH)_2$ nanobelts which serves as sacrificial material deposited on a silicon substrate.[25] The direct solution of the crystallographic structure from diffraction experiments on thin films is extremely challenging due to the limited number of available Bragg peaks and due to the difficulty in extracting exact structure factors from the measured intensities.[37,38,49] Therefore, as a first step, a structural model of the MOF was derived from density functional theory (DFT)-based simulations. The suitability of this crystal structure is then assessed by comparing it to the results of X-ray diffraction experiments. As a complementary approach, measured and simulated IR spectra of the thin films are compared. Based on the suggested crystal structure, as a final step, the texture of the MOF crystallites in the two types of films is determined using pole figures extracted from the rotating-GIXD data. In this way, fundamentally different orientations of the MOFs relative to the substrate surface can be identified for the differently prepared thin films.

## 2. METHODS

**2.1. Experimental Methods.** *2.1.1. Synthesis.* The synthesis of LbL grown $Cu_2(bdc)_2(dabco)$ was based on the procedure presented by McCarthy et al.[50] Thin films were prepared on a cleaned native oxide silicon wafer by two pump sequences alternating between a metal precursor solution ($Cu(CO_2CH_3)_2 \cdot H_2O$ in ethanol) for 15 min and a linker precursor solution (of 1,4-benzenedicarboxylic acid ($H_2bdc$) and dabco in ethanol) for 30 min, including rinsing procedures with ethanol in between. Here, a thin film prepared by 20 cycles is studied. The relevant surface-chemistry is described in ref 50, and there it is also explicitly shown that no functionalization with a surface anchoring molecule on properly cleaned Si substrates is required for obtaining high-quality films.

A second type of sample was prepared by a CtM conversion technique using $Cu(OH)_2$ nanobelts (NBs) as starting points for the MOF growth.[25,51] The chemical synthesis of the NBs is described in the Supporting Information. The crystalline NBs were injected onto a water bath with a syringe, creating an aligned and uniform film.[52] After the deposition, a clean silicon substrate is used for an uptake of the NBs, followed by cleaning with ethanol and drying with nitrogen. The substrate covered by the NBs is subsequently immersed for 1 h at 70 °C


https://doi.org/10.1021/acs.cgd.4c01433
Cryst. Growth Des. 2025, 25, 3665−3679

in 10 mL of methanol-linker solution containing 6.64 mg of $H_2$bdc and 287.1 mg of dabco.[25,52,53] Additionally, a thin film of Cu-bdc (without dabco apical linkers) was grown by an analogous CtM approach, as a reference for identifying certain features in the IR spectra (see below).[25] All samples were stored and investigated in air under ambient conditions. More details are given in the Supporting Information, Section S1.

*2.1.2. Infrared Spectroscopy.* For verifying the structure and composition of the $Cu_2(bdc)_2(dabco)$ films, Fourier transform infrared (FTIR) spectra were recorded using a Bruker ALPHA spectrometer. Measurements in transmission mode were performed under environmental conditions using 64 scans with a resolution of 4 $cm^{-1}$ in the range between 4000 $cm^{-1}$ and 400 $cm^{-1}$. Data analysis and processing were done using the *OPUS* software (version: 8.5).[54] All displayed IR spectra ($I_{tm}$) are baseline-corrected by dividing the measured intensity ($I_{raw}$) by the baseline intensity ($I_{bl}$) (determined with OriginPRO 2021b software[55]): $I_{tm} = \frac{I_{raw}}{I_{bl}}$. The data are presented as absorption spectra ($I_{ab}$) by applying the negative logarithm of the corrected data: $I_{ab} = -\log(I_{tm})$.

*2.1.3. GIXD with Rotating Substrate.* GIXD experiments were performed at beamline XRD1, Elettra, Trieste. The wavelength of the primary X-rays was 1.40 Å, and a Pilatus 2 M detector at a distance of 200 mm from the sample was used to detect the diffracted beam.

A schematic of the experimental geometry is provided in Figure 2. Two angles define the direction of the primary beam relative to that of the sample. The angle of incidence $\alpha_i$ determines the penetration depth and controls the footprint of the primary beam at the sample surface. The incident angles were chosen above the critical angle of $Cu_2(bdc)_2(dabco)$ to ensure full penetration into the MOF thin film. Incident angles of 0.2° and of 0.4° were chosen for the LbL and CtM samples, respectively. The azimuthal direction of the primary beam relative to the substrate is defined by the in-plane angle $\theta_i$ defined around an axis perpendicular to the substrate surface ($z$-axis). The samples were continuously rotated by an overall angle of 360° in 3600 s. The data measured during 10 s were integrated such that we obtained in total 360 2D diffractograms, each covering a range of 1° of $\theta_i$. The integration interval determines the resolution of the diffraction patterns, and the rotation speed is chosen to provide a sufficiently large signal-to-noise ratio. The advantage of the continuous rotation is that it allows the detection of even very sharp diffraction features, e.g., diffraction peaks of single crystal substrates. The rotation of the sample provides access to large volumes of reciprocal space allowing a comprehensive assessment of the crystal structure largely independent of the specific orientation of the crystallites within the thin film samples. Thus, the approach pursued here is much more versatile than GIXD investigations with a static sample, which provide complete diffraction information only for samples with uniplanar texture or randomly distributed crystallites.

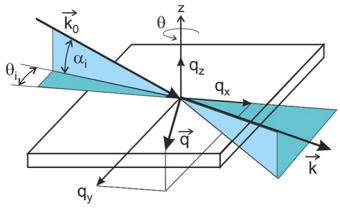


**Figure 2.** Schematic illustration of the geometry of a GIXD experiment with rotating samples (rotating-GIXD). $\vec{k}_0$ and $\vec{k}$ are the wavevectors of the primary and of the diffracted beam, respectively. The incidence angle $\alpha_i$ and the in-plane rotation angle $\theta_i$ define the direction of the primary beam relative to the sample controlling the penetration depth ($\alpha_i$) and the reciprocal space coverage ($\theta_i$). The rotation axis of the sample is along the $z$-direction, perpendicular to the substrate surface. The scattering vector is obtained by $\vec{q} = \vec{k} - \vec{k}_0$. It is used for presenting the diffraction pattern in reciprocal space.

The experimental data were converted to reciprocal space using the software *GIDVis* (version: 2.5), which allows a 3D representation of the diffraction pattern in reciprocal space coordinates.[39] The reciprocal space maps are plotted as a function of the scattering vector $q$ using $q = \frac{4\pi}{\lambda}\sin\theta$ which is separated into an out-of-plane part ($q_z$) and in-plane parts ($q_x$ and $q_y$). The sample coordinate system ($x$ and $y$) is selected in a specific direction so that a simple description of the thin film texture is possible: in particular, for CtM samples, we chose the $x$-axis along the preferred long axis direction of the NBs. Reciprocal space images are also presented for a summation of the intensity during a complete sample rotation. In this case, the in-plane part of the scattering vector is plotted as a function of $q_{xy}$ with $q_{xy}^2 = q_x^2 + q_y^2$.

Before analyzing the data, an intensity correction was performed to overcome instabilities of the primary synchrotron beam. For this purpose, a region of defined size was chosen in the diffuse region between the incident beam and the first Bragg peak. The intensity in this region was averaged and considered as the background, which is then removed from the experimental raw data. These corrected data are further processed in *GIDVis* and corrected in terms of solid angle, pixel distance, detector efficiency, polarization factor (for a 95% polarized primary X-ray beam), and Lorentz factor.[56]

The GIXD results are used for analyzing two crystallographic aspects of $Cu_2(bdc)_2(dabco)$: in a first step, an identification of the crystal structure is performed, and in a second step, the preferred orientation of the crystals relative to the substrate surface (i.e., the texture) is determined. Qualitative phase analysis is performed by comparing the calculated peak pattern directly with the experimental 2D diffraction pattern in reciprocal space coordinates.

Texture analysis is based on pole figures, which are visualizations of the orientations of the crystals. They are based on the direction of net plane normals (also denoted as poles).[57] Since pole directions and scattering vectors have identical directions, the connection of diffraction experiments with crystal orientations is possible. A single pole figure gives the intensity distribution of a defined Bragg peak for different directions of scattering vector $\vec{q}$. The direction of the scattering vector is presented in a circular plot with Euler angles $\phi$ and $\psi$, where $\phi$ denotes the rotation angle around the surface normal of the sample (polar angle) with values in between 0° and 360° and $\psi$ denotes the inclination angle with respect to the surface normal (polar radius) in the range between 0° and 90°.[33] The intensity (or pole density) at each $\phi/\psi$ pair is represented by a color code,[58] with black and yellow representing low and high intensities, respectively.

Pole figures can be computed from the 3D reciprocal space representation of the experimental data. Compared to texture diffractometers, which have to measure individual pole figures for each scattering vector separately, a whole series of pole figures can be computed from rotating-GIXD data. For that, single pole figures are evaluated for a constant value of $|\vec{q}|$, assuming a specific width of $\Delta q$ = 0.005 $Å^{-1}$. The experimental pole figures are compared to calculated stereograms (simulated by *Stereopole* (version: 1.2))[59] based on the crystal lattice under investigation, i.e., based on the lattices of $Cu_2(bdc)_2(dabco)$ or $Cu(OH)_2$, respectively. The obtained textures are assigned on the basis of the classification scheme of Heffelfinger and Burton.[60]

**2.2. Computational Modeling.** The geometry of $Cu_2(bdc)_2(dabco)$ was optimized by using two complementary codes: the FHI-aims code (version: 210716)[61] employing atom-centered basis sets and VASP (version: 6.3.0,[62,63] which combines a plane-wave basis with projector-augmented wave potentials). This was done (i) to show that the obtained results are independent of details of the used methodology and (ii) to utilize specific functionalities readily available in only one of the codes (see below). In these calculations, the Perdew–Burke–Ernzerhof (PBE) functional[64] was combined with two conceptually different van der Waals corrections: the many-body dispersion correction[65,66] in the case of FHI-aims and the Grimme's D3 approach when using VASP.[67] A converged Γ-centered 2 × 2 × 2 k-grid[68] was employed, and the default "tight" basis sets were used in FHI-aims. In VASP, the same k-grid and a 900 eV energy cutoff were chosen (for convergence tests, see Supporting Information).


https://doi.org/10.1021/acs.cgd.4c01433
Cryst. Growth Des. 2025, 25, 3665−3679

Table 1. Lattice Parameters, Volume, and Energy Differences $\Delta E$ for Different Magnetic Configurations of $Cu_2(bdc)_2(dabco)$ Denoted as Nonmagnetic (NM), Ferromagnetic (FM), and Antiferromagnetic (AFM), Calculated Using FHI-Aims and VASP[a]

| | VASP | | | | FHI-aims | | | |
|---|---|---|---|---|---|---|---|---|
| | cell length [Å] | cell angle [°] | volume [Å$^3$] | $\Delta E$ (meV/UC) | cell lengths [Å] | cell angle [°] | volume [Å$^3$] | $\Delta E$ (meV/UC) |
| NM | $a$ = 10.910 | $\alpha$ = 89.23 | 1151.31 | 193.9 | $a$ = 10.905 | $\alpha$ = 90.97 | 1146.68 | 261.3 |
| | $b$ = 10.917 | $\beta$ = 90.79 | | | $b$ = 10.905 | $\beta$ = 90.93 | | |
| | $c$ = 9.663 | $\gamma$ = 91.27 | | | $c$ = 9.648 | $\gamma$ = 88.10 | | |
| FM | $a$ = 10.967 | $\alpha$ = 89.51 | 1153.72 | 60.5 | $a$ = 10.932 | $\alpha$ = 89.87 | 1154.46 | 70.3 |
| | $b$ = 10.967 | $\beta$ = 90.49 | | | $b$ = 10.933 | $\beta$ = 89.88 | | |
| | $c$ = 9.593 | $\gamma$ = 91.01 | | | $c$ = 9.659 | $\gamma$ = 89.41 | | |
| AFM | $a$ = 10.922 | $\alpha$ = 90.58 | 1156.08 | 0.0 | $a$ = 10.919 | $\alpha$ = 90.23 | 1153.92 | 0.000 |
| | $b$ = 10.922 | $\beta$ = 90.56 | | | $b$ = 10.919 | $\beta$ = 90.22 | | |
| | $c$ = 9.692 | $\gamma$ = 89.26 | | | $c$ = 9.680 | $\gamma$ = 89.48 | | |
| AFM | | | | | $a$ = 10.925 | $\alpha$ = 90.0 | 1156.98 | |
| | | | | | $b$ = 10.925 | $\beta$ = 90.0 | | |
| | | | | | $c$ = 9.694 | $\gamma$ = 90.0 | | |

[a]The last entry in the current table provides the unit-cell parameters for the antiferromagnetic configuration with all cell angles fixed at 90°. As explained in the main text, this structure will be used for the further analysis in the remainder of the manuscript. The abbreviation UC means unit cell.

As the $Cu^{2+}$ ions contain unpaired spins, ferromagnetic and antiferromagnetic configurations of the Cu-paddlewheels were optimized. Different spin states in the simulations were achieved by initializing the magnetic moments of the Cu ions and by enforcing total multiplicities of the unit cell of S = 1 (open-shell triplet) and S = 0 (open-shell singlet).[69] For the antiferromagnetic state, the initial magnetic moments of the two copper atoms in each paddlewheel structure were aligned antiparallel. Conversely, for the ferromagnetic state, the copper atoms in the primitive unit cell were initialized, with their spins aligned in parallel. A detailed characterization of the spin states and their impact can be found in Section S2.3 of the Supporting Information. Also, the nonmagnetic (i.e., closed shell singlet) configuration enforcing identical spatial orbitals for the spin-up and spin-down channels was modeled. These simulations reveal an antiferromagnetic ground state of $Cu_2(bdc)_2(dabco)$, as described in the Results and Discussion section.

The optimizations started from the structure of $Zn_2(bdc)_2(dabco)$ as documented in the Cambridge Crystallographic Data Centre, replacing the $Zn^{2+}$ ions by $Cu^{2+}$ ions.[64] Subsequently, both the lattice parameters as well as the atomic positions were fully relaxed using the conjugate gradient algorithm in VASP[70] and an enhanced version of the Broyden−Fletcher−Shanno−Goldfarb (BFGS) algorithm[61] in FHI-aims until the remaining forces fell below $10^{-3}$ eV/Å.[61] Unless specifically stated, all lattice parameters were freely optimized, and no symmetry constraints were imposed (P1 symmetry). In FHI-aims, which straightforwardly allows us to fix unit-cell angles, also a structure with a fully orthogonal unit cell was optimized for the antiferromagnetic configuration.

For calculating vibrational modes with VASP, a finite difference scheme was used employing the Phonopy package,[71] setting the displacements of individual atoms to 0.01 Å. IR intensities were calculated by using Born effective charges obtained through density functional perturbation theory. The process involves determining the oscillator strengths from the Born effective charges[72] and atomic displacement vectors. It is commonly observed for MOFs that the resulting PBE-calculated spectra yield a not fully satisfactory description of vibrations. This is in sharp contrast to spectra of molecular crystals.[73,74] The larger deviations for MOFs are tentatively attributed to the strongly polar nature of their bonds, whose description suffers from the charge over delocalization prevalent in generalized gradient functionals. This can at least in part be mended by the use of hybrid functionals, which have, for example, been successfully applied for modeling the IR spectra of MIL100 and MIL101.[75] For various materials, especially the B3LYP functional has provided a very good agreement with experimental spectra.[76−79] Unfortunately we did not succeed in performing hybrid functional calculations for systems as complex as $Cu_2(bdc)_2(dabco)$ using VASP due to the high computational costs associated with the plane-wave basis set. Thus, the IR spectra presented in the main manuscript were calculated using the CRYSTAL23 code (version: 1.0.1),[80] employing the B3LYP[81,82] functional including Grimmés D3 dispersion correction[67] with Becke-Johnson damping[83] (D3/BJ) together with the VTZP[84] basis set for the linker atoms and the POB-TZVP-rev2[85] basis set for the Zn atoms. The IR spectra discussed in this study were computed based on the fully B3LYP-relaxed structure of $Cu_2(bdc)_2(dabco)$ in the antiferromagnetic state. Frequencies were calculated using numerical first-derivatives obtained from the finite difference formula. An anharmonic correction was applied to stretching vibrations that involve hydrogen atoms.[86] For this, the bond length that involves this type of vibration is varied, and for each distance, the total potential energy is calculated by solving the nuclear Schrödinger equation.[87] Then, a polynomial of sixth order is fitted to these energy points, allowing one to obtain the anharmonicity constants. Further details of the calculations (including convergence tests) can be found in Section S2.4, where IR spectra for the PBE functional calculated with VASP and CRYSTAL23 are also compared to illustrate the fundamental equivalence of the two approaches.

## 3. RESULTS

**3.1. Simulated Crystal Structure.** As $Zn_2(bdc)_2(dabco)$[64,88] has a well characterized structure, which is used as a starting point for the simulations, an isostructural conformation for $Cu_2(bdc)_2(dabco)$ was assumed. The $Zn^{2+}$ ions were replaced by $Cu^{2+}$ ions, to generate a suitable starting point for the geometry optimizations.[89] The experiments suggest that $Zn_2(bdc)_2(dabco)$ adopts a tetragonal structure (space group $P4/mmm$[64]). In full geometry optimizations, marginal deviations from an orthogonality of the lattice vectors were observed, with deviations amounting to a few tenths of a degree. This applies to $Zn_2(bdc)_2(dabco)$ (see Table S2) and to $Cu_2(bdc)_2(dabco)$ (see Table 1). The exact magnitude of these marginal deviations from orthogonality depends on the relative spin-orientation in the Cu paddlewheels and also on the details of the applied methodology (see Table 1). Still, the slightly distorted structures are consistently energetically more stable in all simulated systems, but only by ∼0.02 meV/atom. This suggests that the distortions of the unit cells in the optimizations refer to particularly soft degrees of freedom with corresponding vibrations excited already at rather low temperatures such that one can expect the structures to be "orthogonal on average". Thus, for the following analysis of the experimental GIXD data, an AIMS-calculated structure with a


https://doi.org/10.1021/acs.cgd.4c01433
Cryst. Growth Des. 2025, 25, 3665−3679

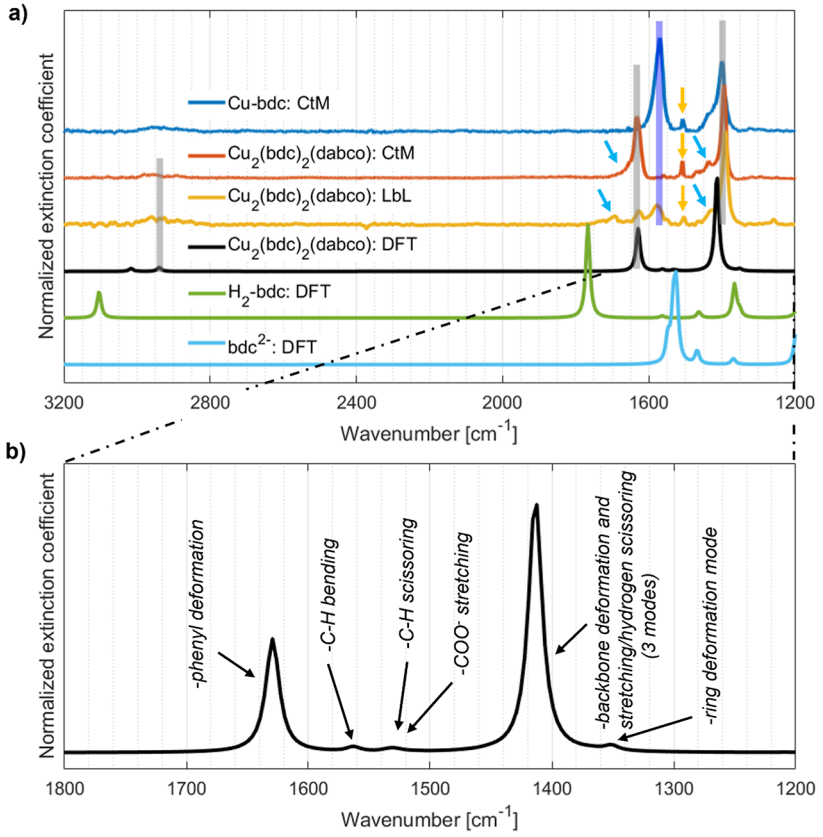


**Figure 3.** Simulated and measured FTIR spectra of $Cu_2(bdc)_2(dabco)$ in the spectral region free of substrate features. Panel (a) compares the experimental result for the ceramic-to-MOF (CtM) sample (red) and for the layer-by-layer (LbL) sample (orange) with simulations on $Cu_2(bdc)_2(dabco)$ crystals assuming a random crystal orientation and correcting for anharmonic effects (black). For the sake of comparison, also the measured spectrum of a CtM grown Cu-bdc film (blue line) and the simulated spectra of an isolated terephthalic acid molecule (bdc linker molecule prior to deprotonation; denoted as $H_2(bdc)$) and its doubly deprotonated dianion (denoted as $bdc^{2-}$) are shown. The vertical, gray lines highlight the main spectral features of $Cu_2(bdc)_2(dabco)$ observed by experiments and in simulations, the vertical blue line denotes the position of the experimental main peak of Cu-bdc, the orange arrows highlight an IR peak associated with bdc dianions (for details see main text), and the cyan arrows denote IR features associated with adsorbates. The Cu-bdc sample shows the same spectrum as reported in ref 25,93. Panel (b) provides a zoom into the calculated spectrum of the most relevant region of panel (a). It shows positions and IR intensities of active vibrations of the simulated $Cu_2(bdc)_2(dabco)$ crystal. Additionally, the nature of the main features are provided (see Table S5).

tetragonal unit cell will be used (see last entry of Table 1; for details on its optimization see Methods section).

Regarding the spin states of the paddlewheels in $Cu_2(bdc)_2(dabco)$, all calculations attest to an antiferromagnetic (open-shell singlet) ground state. This is also fully consistent with the situation in Cu paddlewheels in HKUST-1 both in experiments and simulations.[69,90−92] The spin state, however, has only a very minor impact on the unit cell lengths and volumes. For example, in the FHI-aims simulation results reported in Table 1, the unit cell volumes vary by only ∼0.1% between the antiferromagnetic and the ferromagnetic states.

The calculated lattice parameters of $Cu_2(bdc)_2(dabco)$ for the fully relaxed AFM ground state configuration are $a = b = 10.919$ Å and $c = 9.680$, with $\alpha = 90.230°$, $\beta = 90.217°$, and $\gamma = 89.479°$. They essentially do no change in the case of the tetragonal structure (last set of entries in Table 1). The two crystal structures are provided as a crystallographic information file (cif) as part of the Supporting Information. Compared to $Zn_2(bdc)_2(dabco)$, the lattice constants of $Cu_2(bdc)_2(dabco)$ decreases by 0.1% in both the *a*- and *b*- directions (along the bdc linkers), while the lattice constant increases by 0.8% in the *c* direction (dabco direction) (cf., Table S2).

**3.2. Confirmation of the Simulated Structure.** Two experimental techniques, namely, IR spectroscopy and GIXD, are used to confirm the theoretically determined crystal structure of $Cu_2(bdc)_2(dabco)$. The former identifies the chemical building blocks of the MOF by analyzing molecular vibrations, while the latter probes the unit cell parameters as well as the arrangement of the atomic and molecular building blocks within the crystalline lattice. For both methods, the experimental results will be compared to the theoretical predictions based on the crystal structure determined in the previous section.

*3.2.1. Infrared Spectroscopy.* Figure 3a shows the experimental spectra of both thin film samples and a calculated spectrum of $Cu_2(bdc)_2(dabco)$ crystals assuming an isotropic distribution. For the sake of comparison (see below), also the experimental spectrum of Cu-bdc and the simulated spectra of an isolated terephthalic acid molecule (parent compound of bdc linkers) and of the doubly deprotonated dianion are shown. No data for wavenumbers below 1200 $cm^{-1}$ are displayed in Figure 3a, as IR absorption bands associated with the oxidized Si substrates strongly overlap with $Cu_2(bdc)_2(dabco)$ features, which prevents an unambiguous assignment of the peaks. The full spectra and a detailed analysis on the peaks below 1200 $cm^{-1}$ are provided in Figure S6. The simulations allow an assignment of experimental peaks to specific crystal vibrations, as shown in Figure 3b. The simulated positions of the most relevant IR-


https://doi.org/10.1021/acs.cgd.4c01433
Cryst. Growth Des. 2025, 25, 3665−3679

active modes are also provided in Table S5 together with links to the respective animations.

The two main experimental features in the considered spectral range associated with $Cu_2(bdc)_2(dabco)$ are found at 1393 $cm^{-1}$ and 1633 $cm^{-1}$ (thick gray, vertical lines in Figure 3a), consistent with the results of Baumgartner et al.[93] The experimental peak positions agree well with (i) two essentially degenerate and strongly IR active vibrations simulated for the $Cu_2(bdc)_2(dabco)$ crystal (calculated to be at 1414 $cm^{-1}$) and (ii) with a single band simulated to be at 1629 $cm^{-1}$. It has to be mentioned that the calculated positions of the IR active modes depend on the functional used, as discussed in Section 2.2, while the overall shape of the spectra is not seriously affected. Thus, perfect agreement between simulated and measured peak positions cannot be expected. Still, the good correspondence between simulations and experiments is only observed for the calculated IR spectra of the MOF crystal (black line in Figure 3a), while the respective peaks obtained in the simulations of an isolated terephthalic acid molecule (green line in Figure 3a) are strongly shifted to positions at which no peaks are observed in the experiments. This is the first strong indication that $Cu_2(bdc)_2(dabco)$ crystals are actually formed in the experiments. In particular, the data show that the terminal groups of the ligands participated in the reactions, leading to thin film formation in a manner consistent with the simulated $Cu_2(bdc)_2(dabco)$ crystal structure. The relevance of the IR spectrum of the bdc dianion will be discussed below.

The modes at 1414 $cm^{-1}$ correspond to backbone-stretching vibrations of the bdc linkers accompanied by a scissoring motion of the O−C−O elements, mostly affecting the bonds between the phenylenes and the O−C−O groups. This results in a polarization of the vibrations within the $Cu_2(bdc)_2(dabco)$ planes (see labeling in Figure 3b). The line at 1629 $cm^{-1}$ is dominated by an asymmetric deformation vibration in the phenyl unit of the bdc groups, which is in phase for all respective groups in the crystal. The resulting displacements of the central carbon atoms are parallel to the directions of the dabco linkers such that only IR photons polarized in that direction are absorbed. Thus, the observation that the 1629 $cm^{-1}$ peak in the LbL sample (orange line) is much lower than in the CtM sample is a first indication that the LbL sample grows with the dabco linkers preferentially perpendicular to the substrate,[93] a notion that will later be confirmed by the in-depth analysis of the GIXD data. In the simulations, there are also several weaker IR-allowed vibrations between ∼1300 $cm^{-1}$ and 1700 $cm^{-1}$. Their unambiguous assignment to experimental features is, however, difficult. In contrast, the features found around 3000 $cm^{-1}$ in the simulations can be correlated with the rather broad and weak feature found in the experiments at 2940 $cm^{-1}$. They correspond to C−H stretching vibrations (which are strongly affected by anharmonic effects, see Methods section).

Another prominent feature is the peak found in the LbL spectra at 1577 $cm^{-1}$ (see vertical blue line), which is not observed in the CtM sample. It also does not have an analogue in the simulated spectrum, as the weak simulated features at 1563 $cm^{-1}$ are not intense enough to explain the experimental observations. Thus, we compared the experimental IR spectra of $Cu_2(bdc)_2(dabco)$ to that measured for a Cu-bdc reference sample (shown as the topmost line in Figure 3a; for details, see Methods section). Indeed, the most prominent band in Cu-bdc overlaps with the so far unexplained feature in the spectrum of the LbL prepared $Cu_2(bdc)_2(dabco)$. This implies that in the thin film grown by the LbL technique Cu-bdc crystals are also formed, which do not contain any dabco pillar linkers. Another feature not occurring in the simulated $Cu_2(bdc)_2(dabco)$ spectrum but in all samples containing bdc-linked MOFs is a sharp peak at 1507 $cm^{-1}$ (orange arrow). This feature has also been observed in Baumgartner et al.[93] in all studied bdc-containing MOFs and it has been associated with the "skeletal ring vibration" of bdc. Indeed, we also find a prominent feature in the respective wavenumber range (peaking at 1526 $cm^{-1}$), when calculating an isolated $bdc^{2-}$ dianion (see the light blue curve in Figure 3a). This suggests that all MOF samples contain deprotonated bdc molecules that are not part of the crystalline $Cu_2(bdc)_2(dabco)$ regions and, thus, largely preserve their molecular character, being only loosely associated with (presumably $Cu^{2+}$) counterions to ensure charge neutrality. The shift of around 20 $cm^{-1}$ between the measured and simulated peak positions can be attributed either to the loose interactions with counterions or to the strong methodology-dependence of the simulated peak positions mentioned above.

An unambiguous assignment of the additional peaks and shoulders denoted by the cyan arrows was not possible. In this context, it is, however, worthwhile mentioning that water vapor is known to have vibration−rotation bands in the regions of the cyan arrows. This could be an indication of residual water being present in the samples, potentially in the pores. The water in the pores would, however, need to be extremely weakly bonded such that vibration−rotation bands would occur, as in experiments on water vapors. In passing, it is noted that the IR signatures of vapors of the solvent molecules used in the synthesis (methanol and ethanol) were not observed.

Overall, the IR spectra indicate the successful synthesis of the $Cu_2(bdc)_2(dabco)$ crystals, with the additional presence of amorphous $bdc^{2-}$ containing regions and bands associated with Cu-bdc in the case of the LbL produced films. Further information on the nature of the crystalline constituents of the formed thin films will be obtained from X-ray diffractograms in the next section.

*3.2.2. Phase Analysis via X-ray Diffraction.* The crystallographic phase analysis of both types of thin films is performed by comparing the experimental X-ray diffraction pattern with the calculated pattern based on the theoretically predicted crystal structure of $Cu_2(bdc)_2(dabco)$. The 2D reciprocal space maps for both samples are presented in Figure 4. The left and right sides of the plots (positive and negative $q$ axis) display identical GIXD patterns. Therefore, only one side is used for the phase analysis, while on the other side, the measured features are shown without being covered by the labeling.

The sample grown by the LbL method shows distinct diffraction peaks that are found to be independent of the azimuthal orientation angle (denoted as $\phi$) of the sample. This means that the rotating-GIXD data reveal that the GIXD patterns are indeed independent of the direction of the in-plane scattering vector. Therefore, the intensities for a complete sample rotation are summed, and the notation $q_{xy}$ is used (Figure 4a).

The Bragg peaks appear at defined $q_{xy}/q_z$ positions, which can be unambiguously indexed based on the theoretically predicted crystal structure. The calculated 2D diffraction pattern is based on the assumption that the (001) plane of $Cu_2(bdc)_2(dabco)$ crystals is parallel to the substrate surface; indeed the presence of defined peaks reveals a strong preferred orientation of the crystallites (see also discussion in Section 3.3). Peak positions as well as peak intensities fit well. Notably, the peaks are elongated


https://doi.org/10.1021/acs.cgd.4c01433
Cryst. Growth Des. 2025, 25, 3665−3679

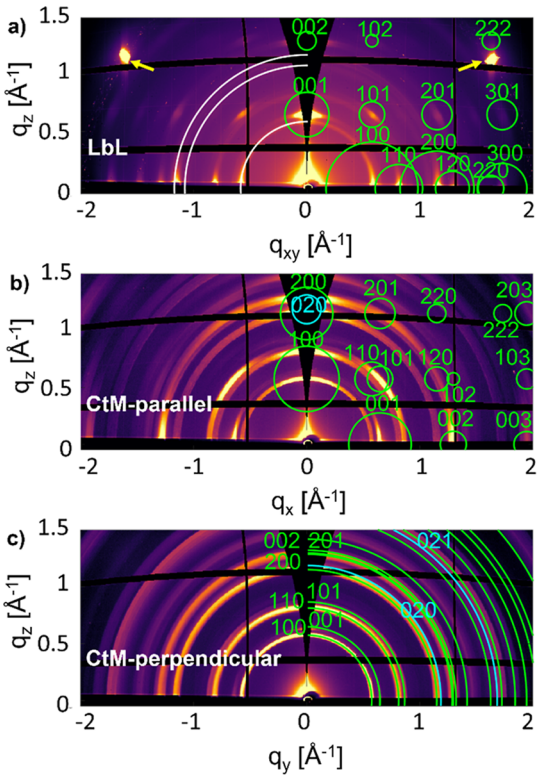


**Figure 4.** Reciprocal space maps of $Cu_2(bdc)_2(dabco)$ prepared (a) by the LbL and (b,c) by the CtM methods. The maps are presented in (a) by integrated intensities for a full sample rotation, the two yellow arrows indicate 111 diffraction peaks from the silicon substrate. The maps (b,c) present specific cuts through reciprocal space (with the *x*-direction aligned along the preferred direction of the long axes of the nanobelts and the *y*-direction being perpendicular to it, see also main text). Calculated peak positions of $Cu_2(bdc)_2(dabco)$, Cu-bdc, and of $Cu(OH)_2$ are given by quater circles in green, white, and cyan color, respectively. Small full circles indicate peak positions (via the centers of the circles) and intensities (via the areas of the circles scaled with the squares of the structure factors). Debye–Scherrer rings - plotted by quarter circles correspond to specific peak positions (a,c).

into arc-type structures indicating an appreciable out-of-plane mosaicity.

For the phase analysis of the CtM sample, two reciprocal space maps are presented: one along the in-plane direction $q_x$ (Figure 4b). Here, the *x*-direction is defined in the sample coordination system as being parallel to the preferred alignment direction of the long axes of the NBs. The second map is aligned along $q_y$, i.e., within the sample surface, but perpendicular to $q_x$ (Figure 4c). Again, it is the availability of the full rotating-GIXD data set that allows us to identify these two GIXD patterns as the ones most relevant for further analysis. In the first map (Figure 4b), diffraction maxima can be identified, although the arc-type structures are more pronounced than those in Figure 4a. Here, for plotting the diffraction maxima associated with the calculated 2D diffraction pattern, we assume a specific alignment of the crystallites with the Cu-bdc planes perpendicular to the plane of the substrate and the dabco linkers aligned along the *x*-direction. In contrast to the situation in Figure 4b, in Figure 4c exclusively Debye–Scherrer rings are observed, and the calculated diffraction patterns are shown by green quater circles. The $q_x$/$q_z$ peak positions in Figure 4b as well as the *q*-values of the Debye–Scherrer rings in Figure 4c can be well explained by the features derived from the theoretically predicted crystal structure of $Cu_2(bdc)_2(dabco)$. Therefore, it is concluded that the same phase is present in both types of thin films (CtM and LbL), and that this phase is consistent with the calculated crystal structure.

To fully understand the structure of the CtM sample, the crystal structure of the NBs used during the thin film preparation process also must be taken into account. The $Cu(OH)_2$ NBs crystallize in the orthorhombic space group $Cmc2_1$ with lattice constants of $a$ = 2.947 Å, $b$ = 10.593 Å, and $c$ = 5.2564 Å.[94,95] In the chosen representation of the diffraction data ($q_x$ and $q_y$ < 2 Å$^{-1}$), the expected position of the 020 peak would overlap with that of $Cu_2(bdc)_2(dabco)$ (Figure 4b) and the same would apply to the Debye–Scherrer ring at 1.684 Å$^{-1}$ (Figure 4c). A more detailed analysis of the crystallographic properties of the $Cu(OH)_2$ substrate is given in Figures S7 and S8.

An identification of Cu-bdc, whose presence in the LbL film has been suggested by the IR spectra, is not straightforward. Nevertheless, despite the overlap in peak positions with $Cu_2(bdc)_2(dabco)$, Cu-bdc could be identified by Debye–Scherrer rings located at $q$ = 0.586 Å$^{-1}$, at 1.172 Å$^{-1}$, and at 1.080 Å$^{-1}$, visualized by white circles in Figure 4a.[25] No trace of Cu-bdc is found for the CtM sample, consistent with the IR data, indicating that by that growth technique, the pure $Cu_2(bdc)_2(dabco)$ MOF was obtained. In this context it is also interesting to note that Brandner at al.[96] reported the spontaneous transformation from $Cu_2(bdc)_2(dabco)$ to Cu-bdc if a $Cu_2(bdc)_2(dabco)$ film is exposed to humid conditions.

The excellent agreement of our experimental and theoretical results reveals that isostructural replacement is a versatile tool for generating guesses for possible crystal structures.[89] In this context, it should, however, be mentioned that $Cu_2(bdc)_2(dabco)$ is a particularly straightforward example and, thus, was also intentionally chosen for portraying the methodology described in the current manuscript. To our experience, in certain cases, the "search space" for starting structures for isostructural replacements needs to be broadened. Also, single-crystal diffraction data of the considered material can provide useful information, even though thin film structures often do not directly correspond to those found in the bulk due to variations in the growth conditions and due to the impact of the substrate triggering the growth of substrate-induced phases.[38,97]

### 3.3. Texture Determination via X-ray Diffraction.

Knowing the crystal structure of $Cu_2(bdc)_2(dabco)$ opens up the possibility of a thorough investigation of the preferred orientation of the crystallites within the thin films. To unambiguously determine the thin film texture, pole figures are used in combination with simulated stereograms based on the investigated crystal phase.[98] A particular advantage of the rotating-GIXD method is that from the obtained data, pole figures for essentially any reflection can be calculated and compared to stereograms computed for the proposed crystal structure of $Cu_2(bdc)_2(dabco)$. This allows the determination of the orientation distribution of the MOF crystallites and, with knowledge of the framework structure relative to the crystallographic lattice, the determination of the orientation of the bdc and dabco linkers.

*3.3.1. Layer-by-Layer Deposited $Cu_2(bdc)_2(dabco)$.* The texture evaluation for the LbL sample was performed using the pole figures of the 001 Bragg peak and the 101 Bragg peak, with scattering vector lengths of $q$ = 0.65 Å$^{-1}$ and $q$ = 0.86 Å$^{-1}$, respectively. The pole figure of the 001 Bragg peak shows a clear peak in the center (Figure 5a), indicating that the (001) crystal


https://doi.org/10.1021/acs.cgd.4c01433
Cryst. Growth Des. 2025, 25, 3665–3679

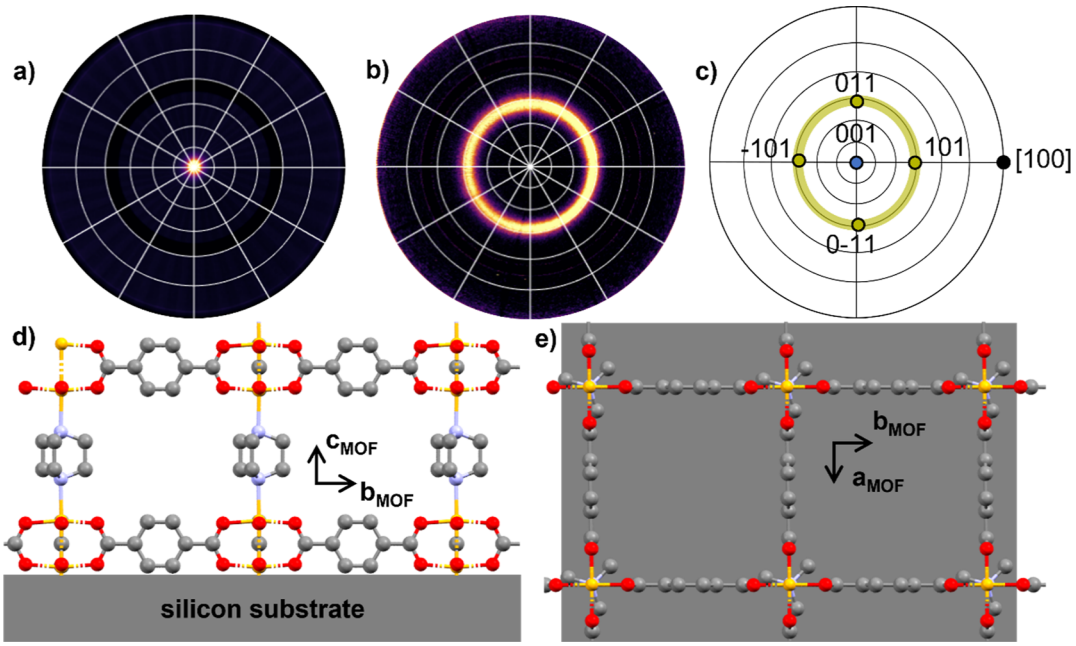


**Figure 5.** X-ray diffraction pole figures (a) of the 001 peak evaluated at $q = 0.65$ Å$^{-1}$ and (b) of the 101 peak evaluated at $q = 0.86$ Å$^{-1}$. Image (c) shows the calculated stereogram with the 001 pole in the center and the 101 poles at a tilt angle of $\psi = 41.7°$. The ring is characteristic for a uniplanar texture. The images (d,e) illustrate the extracted framework structure of $Cu_2(bdc)_2(dabco)$ relative to the substrate surface in side and top view. The crystallographic axes indicate the crystal orientation of the MOF relative to the substrate surface. The brown, red, gray, and blue spheres show the copper, oxygen, carbon, and nitrogen atoms. The atomic arrangement is plotted with the visualization software Mercury from Cambridge Crystallographic Data Center.

plane is parallel to the substrate surface. This is consistent with analysis of the GIXD pattern (Figure 5a). In contrast, the pole figure of the 101 Bragg peak exhibits a circular shape (Figure 5b). Both pole figures are compared with the calculated stereogram (Figure 5c) of a single $Cu_2(bdc)_2(dabco)$ crystal, assuming that it is aligned with the 001 pole perpendicular to the plane of the plot and the [100] direction parallel to its horizontal axis. Only the poles for the (001) plane and the {101} equivalent planes (namely, (101), (011), (−101), and (0−11)) are shown. The experimentally observed pole directions with high intensities (Figure 5a,b) agree with the calculated stereogram concerning their polar radii of $\psi = 0°$ for the 001 and $\psi = 41.7°$ for the 101 poles. However, the ring-like feature of the 101 pole figure (Figure 5b) is clearly different from the four individual directions of the poles corresponding to the (101), (011), (−101), and (0−11) planes present in the stereogram at defined polar angles ($\phi = 0°$, 90°, 180°, and 270°). This implies that the thin film consists of crystallites with random azimuthal orientation relative to the normal of the substrate surface. This is expected,[99] considering that the samples are grown on isotropic substrates. The fact that the crystals are aligned with the (001) planes parallel to the substrate but lack any in-plane alignment allows us to classify the distribution of the $Cu_2(bdc)_2(dabco)$ crystals as uniplanarly textured.[60] The Debye−Scherrer ring at $q = 1.08$ Å$^{-1}$ associated with the Cu-bdc phase indicates that this phase displays random texture;[60] a more detailed analysis of this unintended structure goes beyond the scope of the present paper.

Knowing the experimentally observed preferred orientation of the $Cu_2(bdc)_2(dabco)$ crystals, the orientation of the linker molecules within the crystal structure can be identified, and the network structure of the MOF relative to the substrate surface can be determined. It is shown in a side view in Figure 5d and in a top view in Figure 5e: the dabco-linkers are oriented perpendicular to the substrate surface, while the bdc-linkers are arranged in a plane parallel to the substrate surface.

The uniplanar texture of the LbL film is associated with the absence of any in-plane order of the $Cu_2(bdc)_2(dabco)$ crystallites; this is in agreement with the isotropic thin film microscope images. Disordered elongated plates with a lateral size between 200 and 600 nm and flakes with a size of about 1 $\mu$m are observed in good agreement with the results of McCarthy et al.[50] The images are depicted in the Supporting Information, Figure S1a.

*3.3.2. Ceramic-to-MOF Grown $Cu_2(bdc)_2(dabco)$.* The texture of the crystals in the CtM sample is also determined by using pole figures. Pole figures of the 100 Bragg peak (Figure 6a) and the 101 Bragg peak (Figure 6b) are generated with scattering vector lengths of $q = 0.58$ Å$^{-1}$ and $q = 0.86$ Å$^{-1}$, respectively. To obtain the orientation of the crystals, the pole figures are again compared with a calculated stereogram (Figure 6c). For the stereogram, a single crystal is aligned with the [001] direction parallel to the horizontal direction (i.e., $x$ = axis) of the plot. The blue circles denoted as 0−10, 100, and 010 are obtained assuming the 100 poles of the $Cu_2(bdc)_2(dabco)$ crystals perpendicular to the plane of projection (i.e., parallel to the $z$-axis). Provided that crystallites can rotate freely around the [001] axis, the poles of the {100} planes are distributed over multiple directions, as illustrated by the thick blue line in Figure 6c. In such a case, the [001] axis is referred to as the fiber axis. For the sake of comparison, Figure S10b shows the positions in stereographic projection calculated for specific degrees of rotation. Based on the positions of the poles of the {101} planes, one can estimate the positions of the respective poles for crystallites randomly rotated around the [001] axis. This is indicated by the yellow lines in Figure 6c. For illustrative purposes, the respective poles of one crystal, the one with the (100) plane parallel to the substrate surface, are represented by


https://doi.org/10.1021/acs.cgd.4c01433
Cryst. Growth Des. 2025, 25, 3665−3679

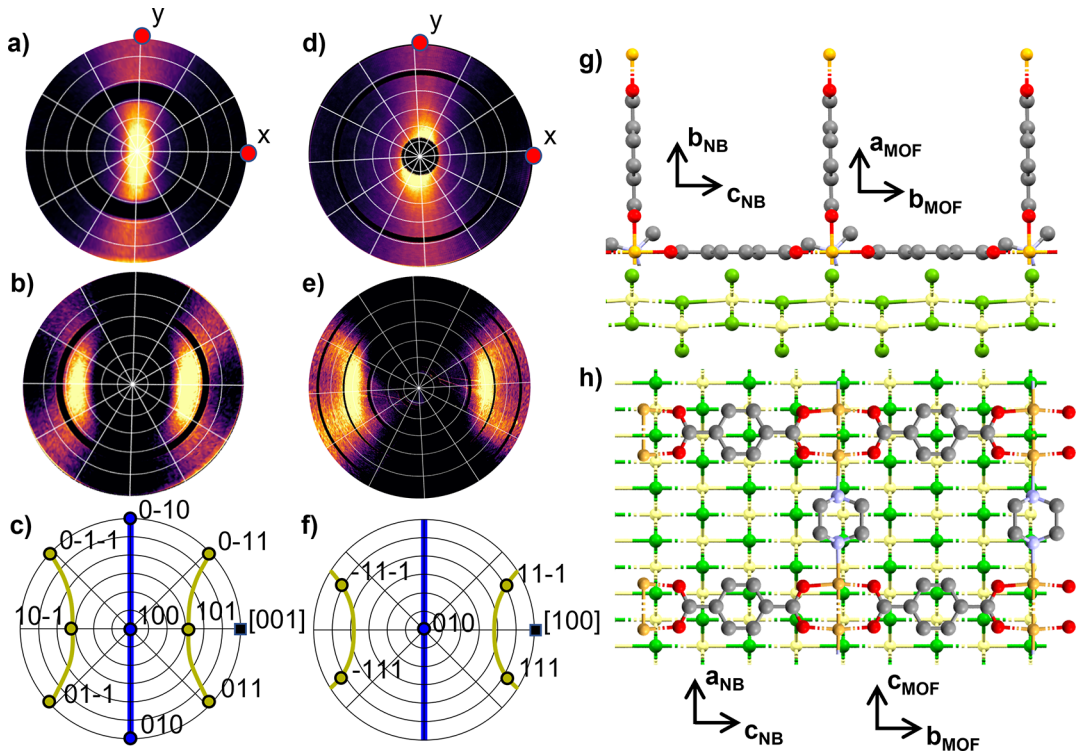


**Figure 6.** Panels (a,b) show X-ray diffraction pole figures of $Cu_2(bdc)_2(dabco)$ of (a) the 100 peak taken at $q = 0.58$ Å$^{-1}$, and (b) the 101 peak taken at $q = 0.86$ Å$^{-1}$; the red dots give the $x$ and $y$ directions of the sample coordinate system. The black rings in the pole figures correspond to the blind spots of the detector. Panel (c) shows the stereogram for an ideal axial texture; the crystals are aligned with the [001] direction along the azimuthal fiber axis. Only the poles of the equivalent {100} and the {101} planes are plotted. Rotating the crystal around the [001] axis yields pole directions of {100} along the blue line and {101} poles along the yellow lines. Panels (d,e) show X-ray diffraction pole figures of $Cu(OH)_2$ nanobelts of (d) the 020 peak taken at $q = 1.18$ Å$^{-1}$, (e) the 111 peak taken at $q = 2.52$ Å$^{-1}$, and (f) the stereogram of an axial texture with [100] as unique direction, for (010) (blue) and for {111} equivalent poles (yellow). The rightmost panels illustrate the epitaxial order of $Cu_2(bdc)_2(dabco)$ crystals at a (010) $Cu(OH)_2$ surface plotted in (g) side view and (h) top view. The green and yellow spheres show the oxygen atoms and the copper atoms of the $Cu(OH)_2$ nanobelt, respectively. The brown, red, gray and blue spheres show the copper, oxygen, carbon and nitrogen atoms of the MOF. The atomic arrangement is plotted with the visualization software Mercury from Cambridge Crystallographic Data Center.

black circles. The calculated stereogram corresponds to an axial texture according to the classification of Heffelfinger and Burton.[60]

The measured pole figures and the stereogram calculated for an ideal axial texture are correlated but do not match perfectly. First, the measured intensity distributions do not follow the theoretically estimated distributions (represented by the blue and yellow lines in the stereograms). They also show an angular spread (i.e., the features are broader than those ideally expected). Second, the observed intensities are not evenly distributed along the calculated directions of the stereogram. Both observations are related to a deviation of the alignment of the $Cu_2(bdc)_2(dabco)$ crystals from the assumed equal distribution around the fiber axis.

The first deviation can be explained by a certain degree of misalignment of the [001] directions of the individual crystals relative to the ideal fiber axis. The angular spread of the [001] axes of the crystallites relative to the ideal fiber axis can be determined from the in-plane mosaicity. The corresponding $\phi$-scan of the 100 Bragg peaks depicted in Figure S11 measures the in-plane mosaicity by the full width at half-maximum (fwhm) of the observed intensity curves. For $Cu_2(bdc)_2(dabco)$ and for $Cu(OH)_2$, average values of 43.9° and 41.9° are found.

For the second mentioned deviation, the reason is a certain preference for the orientation of the crystallites with their (100) planes parallel to the substrate surface. A quantification of this observation by the out-of-plane mosaicity is difficult to perform since the 100 Bragg peak is not accessible for the entire range due to the blind spot of the detector. A clear experimental evidence for a preferred (100) orientation of the crystallites is, however, discussed in the context of Figure S12 in the Supporting Information. From the above arguments, it can be concluded that a considerable fraction of the crystallites is oriented with the (100) plane parallel to the substrates surface, which is a distinct deviation from an ideal axial texture.

A similar texture analysis can be performed on the crystalline $Cu(OH)_2$ NB precursor. The same data set from the rotating-GIXD experiment can be used since the X-ray diffraction features of the MOF and of the NBs are observed simultaneously, but at different $q$-values. Figure 6d and 6e shows the pole figures of $Cu(OH)_2$ taken at the 020 peak ($q = 1.18$ Å$^{-1}$) and at the 111 peak ($q = 2.52$ Å$^{-1}$). Figure 6f illustrates the calculated stereogram for $Cu(OH)_2$ crystals by assuming an ideal axial texture around the [100] direction as fiber axis. Comparison of the pole figures with the calculated stereogram again reveals clear similarities to but also deviations from an ideal axial texture. As in the case of $Cu_2(bdc)_2(dabco)$ crystals, these deviations are caused by a non-ideal fiber texture arrangement of the $Cu(OH)_2$ crystallites. We consider this distinct deviation from an axial texture to be triggered by the plate-like geometry of the NBs,[25,52] which favors the orientation of the large faces of the plates parallel to the substrate. In passing, we note that the



https://doi.org/10.1021/acs.cgd.4c01433
Cryst. Growth Des. 2025, 25, 3665−3679

texture of the NBs prior to the MOF growth is essentially the same as that of the remaining belts in the CtM films, as shown in Figures S7 and S8 for comparison.

The textures of $Cu_2(bdc)_2(dabco)$ and of the $Cu(OH)_2$ NBs show two identical features: (i) the fiber axis preferentially points in identical directions and (ii) a specific crystallographic plane shows a preferred alignment parallel to the substrate surface. Comparing the out-of-plane mosaicities as well as the in-plane mosaicities reveals that the degree of disorder of the $Cu_2(bdc)_2(dabco)$ crystallites is only slightly larger than those of the $Cu(OH)_2$ NBs (compare Figures S11 and S12). This suggests an epitaxial relationship between the $Cu_2(bdc)_2(dabco)$ crystals and the $Cu(OH)_2$ NBs. In fact, the stereogram in Figure 6c,f reveals that $[001]_{MOF}$ (the direction of the dabco molecules) is parallel to $[100]_{NBs}$ (the long axis of the NBs). Moreover, from the preferred orientation of the crystals parallel to the substrate surface, it can be concluded that the {100} planes of the MOFs (i.e., $(100)_{MOF}$ and $(010)_{MOF}$) are preferably parallel to $(010)_{NB}$. This means that these MOF planes, composed of bdc linkers in one direction and dabco linkers perpendicular to it, are parallel to the flat surface of the NBs.

As a consequence, one set of bdc-linkers is perpendicular to the flat $Cu(OH)_2$ NB surface (010 plane) (Figure 6g) and the second set of bdc-linkers, as well as the dabco-linkers, are parallel to it. The lattice mismatches $m_1$ and $m_2$ of the epitaxial thin film in both directions can be calculated according to[100]

$$m_1 = \frac{2c_{NB} - b_{MOF}}{b_{MOF}} \times 100\% \text{ and}$$

$$m_2 = \frac{4a_{NB} - c_{MOF}}{c_{MOF}} \times 100\%$$

Two and four repeat units of the underlying $Cu(OH)_2$ substrate are covered by the bdc- and dabco-linkers, respectively; leading to commensurable lattices.[101] Here, $c_{NB}$ and $b_{MOF}$ are the unit cell parameters along the short axis of the $Cu(OH)_2$ NBs and in the direction of a bdc-linker (Figure 6gh). The unit cell parameters $a_{NB}$ and $c_{MOF}$ are aligned in the direction of the long axis of the $Cu(OH)_2$ NBs and in the direction of the dabco linkers (Figure 6h). The resulting lattice mismatches amount to $m_1 \sim 3\%$ and $m_2 \sim 8\%$, respectively. In this context it is worth noting that, values of mismatches below 10% are taken as tolerance for expecting heteroepitaxial growth of MOFs.[102]

The preferred alignment of the crystallites is in line with the experimentally observed fiber texture of the $Cu_2(bdc)_2(dabco)$ crystallites discussed above.[25] The thin film shows elongated structures aligned preferably in one direction with a characteristic length of about 3 $\mu$m and a width of 0.6 $\mu$m; the result is shown in the Supporting Information, Figure S1b. In this context, it is also worth noting that the orientation, homogeneity, and size of the MOF crystals in the CtM case strongly depend on the pursued synthesis protocol, the thickness of the sacrificial $Cu(OH)_2$ layer, the concentration of reagents, and the possible use of modulators, with all aspects offering ways for improving the film growth.[26,30,103] For the sake of comparison, an optical microscopy image of the aligned $Cu(OH)_2$ NBs for a larger surface area is shown in the Supporting Information, Figure S9b.

## 4. DISCUSSION

The solution of a crystal structure from a thin film is a difficult task, considering the comparably small number of detectable diffraction peaks. The presence of pronounced crystalline textures further complicates access to comprehensive diffraction data. Here, rotating-GIXD experiments (augmented by ab initio simulations) turn out to be a particularly useful tool, providing straightforward access to a detailed analysis of thin film textures and to diffraction peaks in the majority of reciprocal space. In contrast, GIXD experiments with static samples provides only a 2D cut through reciprocal space, which provides only sufficient information to characterize the orientation distribution of the crystallites only in specific cases (i.e., uniplanar or random textures).[60]

The potential of the rotating-GIXD approach is demonstrated by analyzing the crystallographic properties of $Cu_2(bdc)_2(dabco)$ thin films. A model for the crystal structure of $Cu_2(bdc)_2(dabco)$ is obtained based on the documented structure of $Zn_2(bdc)_2(dabco)$ (depicted in Figure 1) by isostructural replacement.[89] This is a particularly promising strategy for MOFs, as for this materials class, isomorphism has frequently been reported.[104−106] In a subsequent step, the suggested geometry is optimized by DFT.[61] The IR spectra calculated for that 3D $Cu_2(bdc)_2(dabco)$ structure are consistent with the experimental data. For the LbL grown films, the measured IR data as well as XRD reveal additionally the presence of Cu-bdc crystallites (Figures 3 and 4a).

The calculated crystal structure is also found to be consistent with the X-ray diffraction experiments. In the case of the LbL sample, discrete Bragg peaks are observed in the GIXD patterns, which are independent of the azimuthal alignment of the sample (Figure 4a). These findings reveal that a uniplanar texture of the crystallites is present.[60] This type of crystal orientation is frequently also denoted as "2D powder".[107,108] When calculating the peak pattern assuming a uniplanar texture with the (001) planes of the MOF crystals parallel to the substrate surface, an excellent agreement between the calculated and measured GIXD patterns is observed. For that texture, the direction of the dabco linker is perpendicular to the substrate surface, as depicted in Figure 5d.

A schematic picture of the orientation of the crystals relative to the substrate surface is given in Figure 7a.

In the case of the CtM sample, the diffraction pattern is strongly dependent on the azimuthal alignment of the sample (Figure 6b,c). Peak patterns with arc-type structures as well as Debye−Scherrer rings appear. The observed anisotropy in an individual GIXD pattern would be consistent with films with preferred in-plane aligned crystallites or with samples with weak statistics.[109,110] A full texture analysis is, however, not feasible based on a single GIXD image. Thus, it is necessary to collect GIXD patterns while systematically varying the azimuthal alignment of the sample (rotating-GIXD). This provides information on a large volume of the 3D reciprocal space, which can be presented in different ways.

For example, from the 3D reciprocal space mapping, pole figures can be calculated for the individual diffraction peaks. Plotting the peak intensities at a defined $q$-value as a function of the polar angles and radii (i.e., $\phi$ and $\psi$) yields pole figures, which are the basis of crystal texture analysis.[111] In the case of the CtM sample, an axial texture together with a tendency to realize biaxially aligned crystals can be identified by comparing pole figures (Figure 6a,b) with calculated stereograms (Figure



https://doi.org/10.1021/acs.cgd.4c01433
Cryst. Growth Des. 2025, 25, 3665−3679

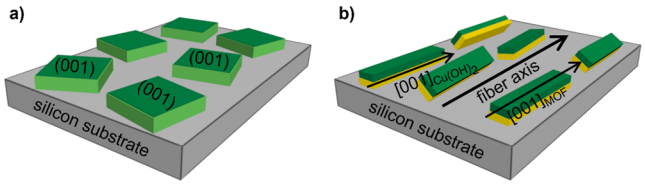


**Figure 7.** Schematic picture for the texture of $Cu_2(bdc)_2(dabco)$ crystals within thin films. Panel (a) shows the uniplanar texture with the crystallographic (001) plane parallel to the substrate surface for the LbL grown film. Panel (b) illustrates the axial texture of the $Cu_2(bdc)_2(dabco)$ crystals (green) epitaxially grown on the $Cu(OH)_2$ (yellow). The crystallographic [001] direction of the $Cu_2(bdc)_2(dabco)$ crystals (corresponding to the axes of the dabco molecules) is aligned with the [100] direction of $Cu(OH)_2$ (the long axes of the nanobelts). Both axes are (close to) parallel to a fiber axis, which is directed along a specific azimuthal direction of the substrate surface defined during the deposition of the nanobelts. The planes of the nanobelts have a certain preference to be aligned parallel to the substrate surface, but nanobelts (and MOF crystals) with all possible rotations around the fiber axis are observed.

6c). Additionally, the underlying $Cu(OH)_2$ NBs can be analyzed by pole figures, since they give rise to Bragg peaks at positions different from those arising from the $Cu_2(bdc)_2(dabco)$ crystallites. Notably, for the $Cu(OH)_2$ NBs, a type of texture comparable with the one for the MOF crystallites is observed (Figures 6d–f and S8c–e). The similarity of the textures indicates that the texture of $Cu_2(bdc)_2(dabco)$ is induced during film growth by the orientation of the $Cu(OH)_2$ NBs serving as sacrificial substrates. This is illustrated in Figure 7b.

The advantages of using rotating samples during the GIXD experiment are clearly apparent by the evaluation of the experimental data by pole figures. Still there are also clear limitations of the method. The peak collection strategy provides a common diffraction pattern of the thin film together with the substrate, e.g., in the case of the LbL sample, a peak stemming from the silicon substrate is also clearly visible (compare Figure 4a). In the present case, the separation of these two peak patterns can be easily performed, but it could be challenging in the case of low symmetry substrates (e.g., for muscovite substrates).[112] It also should be mentioned that GIXD in general is limited by (i) specific areas where diffraction data are not accessible (compare Figure 4, e.g., along $q_z$ at $q_{xy} = 0$ Å$^{-1}$), (ii) diffraction peaks potentially having low resolution due to enhanced peak width, and by (iii) sparse diffraction patterns which are difficult to index. Notably, regarding the latter, significant progress has been made in recent years in the context of automatized indexing,[113] sometimes also based on a machine learning-assisted peak assignment.

When trying to understand the origin of the fundamentally different textures of the two types of films, specific structural features of the substrate surface play a crucial role: The LbL sample is deposited on an oxidized silicon wafer, which forms an atomically flat but amorphous surface with isotropic character. Correspondingly, the two equivalent crystallographic directions of the MOF crystallites containing the bdc linkers (i.e., $[100]_{MOF}$ and $[010]_{MOF}$) do not display any preferred in-plane alignment (Figure 5c). The observation that the (001) plane of the crystallites is parallel to the $SiO_2$ surface is tentatively attributed to the fact that such a texture is consistent with the formation of intact Cu-paddlewheels. Moreover, it is expected to maximize the van der Waals contact area between the substrate surface and the MOF. In the case of the CtM sample, an epitaxial alignment of the bdc and dabco linkers relative to the $(010)_{NB}$ plane of the $Cu(OH)_2$ substrates is found (Figure 6g,h), with the bdc molecules aligned along $[010]_{NB}$ and the dabco linkers aligned along $[001]_{NB}$. Lattice mismatches between $Cu_2(bdc)_2(dabco)$ and the $Cu(OH)_2$ substrates of 8% and 3% are observed, which is consistent with observations for other epitaxial MOF heterostructures.[102,114,115] Both lattice mismatches still allow a favourable atomic arrangement of the MOF and the $Cu(OH)_2$ layers (Figure 6g,h).

As far as the impact of the different textures is concerned, it is interesting to mention that in the case of the LbL film, the extension of the pores parallel to the substrate surface is slightly larger than in the case of the CtM sample (compare Figure 5e with Figure 6h), which might have an impact on the diffusion of guest molecules through the films. Moreover, in a recent study, the use of polar apical linkers to generate gradients of the electrostatic energy has been suggested[116] and (to some extent) also realized experimentally employing LbL growth.[117] In such MOFs, the texture of the films determines the direction of the energy gradients. Moreover, when using optical chromophores as linkers, controlling the texture can be used to obtain polarized absorption and emission properties.[118,119]

## 5. CONCLUSIONS

This work shows, for the example of $Cu_2(bdc)_2(dabco)$, how the crystal structure of thin film MOFs can be solved by starting from an isostructural compound (here: $Zn_2(bdc)_2(dabco)$) and subsequently combining theoretical simulation and experiments. To unambiguously confirm the structure suggested by isostructural replacement, IR spectroscopy as well as GIXD experiments are used. In the case of GIXD, it proves useful to map diffraction peaks in an as large as possible volume of reciprocal space. This can be achieved by the rotating-GIXD approach, recording GIXD patterns while rotating the thin film sample. This was done for two different types of $Cu_2(bdc)_2(dabco)$ films, prepared either by an LbL approach or via CtM conversion starting from aligned $Cu(OH)_2$ NBs as substrates. To interpret the X-ray diffraction data for the thin films, certain textures of the films have to be assumed, which are later confirmed by pole figures directly extracted from the GIXD experiments. On the basis of these, identical crystal structures can be identified in both types of samples. Thin film preparation using the LbL technique results in a uniplanar texture with the (001) plane parallel to the substrate surface. In the case of CtM thin film preparation, a distorted axial texture is observed. In fact, crystals of the $Cu_2(bdc)_2(dabco)$ MOF are found to grow epitaxially on the $Cu(OH)_2$ NBs with the epitaxial relations $[001]_{MOF}\|[100]_{NBs}$ and $\{100\}_{MOF}\|(010)_{NBs}$. These results show that in the two types of thin films, different alignments of the linker framework relative to the substrate surface are found. For the LbL grown films, the isotropic nature of the substrate surface is in accordance with the fact that both bdc-linkers are parallel to the substrate. When CtM conversion is employed, lattice matching between the MOF and the NB substrates leads to a fundamentally different texture with one bdc-linker and one dabco-linker parallel to the substrate surface. As its most important outcome, this work illustrates that GIXD with rotating substrates is a valuable tool for solving the crystal structure of thin films consisting of highly textured crystallites.


https://doi.org/10.1021/acs.cgd.4c01433
Cryst. Growth Des. 2025, 25, 3665−3679

## ■ ASSOCIATED CONTENT

### Data Availability Statement

All original data can be accessed via repository of the Graz University of Technology (DOI 10.3217/87rsq-wey67).

### Supporting Information

The Supporting Information is available free of charge at https://pubs.acs.org/doi/10.1021/acs.cgd.4c01433.

Additional details on thin film preparation and computational tests on geometry optimization; crystallographic characterization of pristine $Cu(OH)_2$ NBs; calculation on the magnetic order and IR spectra; and out-of-plane mosaicities of $Cu(OH)_2$ and the MOF (PDF)

Animations of the molecular vibrations (ZIP)

### Accession Codes

Deposition Nos. 2391759 and 2406443 contain the supplementary crystallographic data for this paper. These data can be obtained free of charge via the joint Cambridge Crystallographic Data Centre (CCDC) and Fachinformationszentrum Karlsruhe Access Structures service.

## ■ AUTHOR INFORMATION


### Corresponding Authors

**Egbert Zojer** − *Institute of Solid State Physics, Graz University of Technology, 8010 Graz, Austria;* orcid.org/0000-0002-6502-1721; Email: egbert.zojer@tugraz.at

**Roland Resel** − *Institute of Solid State Physics, Graz University of Technology, 8010 Graz, Austria;* orcid.org/0000-0003-0079-3525; Email: roland.resel@tugraz.at

### Authors

**Mario Fratschko** − *Institute of Solid State Physics, Graz University of Technology, 8010 Graz, Austria;* orcid.org/0009-0005-2866-0064

**Nina Strasser** − *Institute of Solid State Physics, Graz University of Technology, 8010 Graz, Austria*

**Narges Taghizade** − *Institute of Solid State Physics, Graz University of Technology, 8010 Graz, Austria*

**Mercedes Linares-Moreau** − *Institute of Physical and Theoretical Chemistry, Graz University of Technology, 8010 Graz, Austria;* orcid.org/0000-0003-3027-6238

**Jan C. Fischer** − *Institute of Microstructure Technology, Karlsruhe Institute of Technology, 76344 Eggenstein-Leopoldshafen, Germany*

**Tonghan Zhao** − *Institute of Microstructure Technology, Karlsruhe Institute of Technology, 76344 Eggenstein-Leopoldshafen, Germany;* orcid.org/0000-0002-5300-1651

**Ian A. Howard** − *Institute of Microstructure Technology, Karlsruhe Institute of Technology, 76344 Eggenstein-Leopoldshafen, Germany*

**Paolo Falcaro** − *Institute of Physical and Theoretical Chemistry, Graz University of Technology, 8010 Graz, Austria;* orcid.org/0000-0001-5935-0409

Complete contact information is available at: https://pubs.acs.org/10.1021/acs.cgd.4c01433


### Notes

The authors declare no competing financial interest.

## ■ ACKNOWLEDGMENTS

This research was funde in part by the Austrian Science Fund (FWF) [10.55776/P34463]. For the purpose of open access, the author has applied a CC BY public copyright licence to any Author Accepted Manuscript version arising from this submission. The authors thank the Graz University of Technology [Lead Project LP-03: Porous Materials @ Work for Sustainability] for financial support. The authors acknowledge support from the European Research Council under the European Union's Horizon 2020 Programme (FP/2014-2020)/ERC Grant Agreement No. 771834—POPCRYSTAL. The authors acknowledge Elettra Synchrotron Trieste for allocating beamtime at beamline XRD1. I.A.H., T.Z., and J.F. acknowledge funding through the DFG program SPP 1928 COORNETS, as well as the Helmholtz Association for funding through the MTET program (Materials and Technologies for the Energy Transition)—Topic 1—Photovoltaics (38.01.05). The authors thank Bartolomeo Civalleri from the University of Turin for support with the IR simulations.

## ■ REFERENCES


(1) Furukawa, H.; Cordova, K. E.; O'Keeffe, M.; Yaghi, O. M. The Chemistry and Applications of Metal-Organic Frameworks. *Science* **2013**, *341* (6149), 1230444.

(2) Ding, M.; Cai, X.; Jiang, H.-L. Improving MOF Stability: Approaches and Applications. *Chem. Sci.* **2019**, *10* (44), 10209−10230.

(3) Hong, A. N.; Yang, H.; Bu, X.; Feng, P. Pore Space Partition of Metal-Organic Frameworks for Gas Storage and Separation. *EnergyChem.* **2022**, *4* (4), 100080.

(4) Fan, W.; Zhang, X.; Kang, Z.; Liu, X.; Sun, D. Isoreticular Chemistry within Metal−Organic Frameworks for Gas Storage and Separation. *Coord. Chem. Rev.* **2021**, *443*, 213968.

(5) Chen, G.; Liu, G.; Pan, Y.; Liu, G.; Gu, X.; Jin, W.; Xu, N. Zeolites and Metal−Organic Frameworks for Gas Separation: The Possibility of Translating Adsorbents into Membranes. *Chem. Soc. Rev.* **2023**, *52* (14), 4586−4602.

(6) Khan, I.; Altaf, A.; Sadiq, S.; Khan, S.; Khan, A.; Khan, S.; Humayun, M.; Khan, A.; Abumousa, R. A.; Bououdina, M. Towards Sustainable Solutions: Comprehensive Review of Advanced Porous Materials for $CO_2$ Capture, Hydrogen Generation, Pollutant Degradation, and Energy Application. *Chem. Eng. J. Adv.* **2025**, *21*, 100691.

(7) Mallakpour, S.; Nikkhoo, E.; Hussain, C. M. Application of MOF Materials as Drug Delivery Systems for Cancer Therapy and Dermal Treatment. *Coord. Chem. Rev.* **2022**, *451*, 214262.

(8) Moharramnejad, M.; Ehsani, A.; Shahi, M.; Gharanli, S.; Saremi, H.; Malekshah, R. E.; Basmenj, Z. S.; Salmani, S.; Mohammadi, M. MOF as Nanoscale Drug Delivery Devices: Synthesis and Recent Progress in Biomedical Applications. *J. Drug Delivery Sci. Technol.* **2023**, *81*, 104285.

(9) Wu, M.-X.; Yang, Y.-W. Metal−Organic Framework (MOF)-Based Drug/Cargo Delivery and Cancer Therapy. *Adv. Mater.* **2017**, *29* (23), 1606134.

(10) Hu, G.; Liu, Q.; Deng, H. Space Exploration of Metal−Organic Frameworks in the Mesopore Regime. *Acc. Chem. Res.* **2025**, *58* (1), 73−86.

(11) Dolgopolova, E. A.; Rice, A. M.; Martin, C. R.; Shustova, N. B. Photochemistry and Photophysics of MOFs: Steps towards MOF-Based Sensing Enhancements. *Chem. Soc. Rev.* **2018**, *47* (13), 4710−4728.

(12) Sohrabi, H.; Ghasemzadeh, S.; Ghoreishi, Z.; Majidi, M. R.; Yoon, Y.; Dizge, N.; Khataee, A. Metal-Organic Frameworks (MOF)-Based Sensors for Detection of Toxic Gases: A Review of Current Status and Future Prospects. *Mater. Chem. Phys.* **2023**, *299*, 127512.

(13) Cheng, W.; Tang, X.; Zhang, Y.; Wu, D.; Yang, W. Applications of Metal-Organic Framework (MOF)-Based Sensors for Food Safety:

Enhancing Mechanisms and Recent Advances. *Trends Food Sci. Technol.* **2021**, *112*, 268−282.
(14) Rostamnia, S.; Xin, H.; Nouruzi, N. Metal−Organic Frameworks as a Very Suitable Reaction Inductor for Selective Solvent-Free Multicomponent Reaction: IRMOF-3 as a Heterogeneous Nanocatalyst for Kabachnik−Fields Three-Component Reaction. *Microporous Mesoporous Mater.* **2013**, *179*, 99−103.
(15) Downes, C. A.; Marinescu, S. C. Electrocatalytic Metal−Organic Frameworks for Energy Applications. *ChemSusChem* **2017**, *10* (22), 4374−4392.
(16) Konnerth, H.; Matsagar, B. M.; Chen, S. S.; Prechtl, M. H. G.; Shieh, F.-K.; Wu, K. C.-W. Metal-Organic Framework (MOF)-Derived Catalysts for Fine Chemical Production. *Coord. Chem. Rev.* **2020**, *416*, 213319.
(17) Amenaghawon, A. N.; Anyalewechi, C. L.; Osazuwa, O. U.; Elimian, E. A.; Eshiemogie, S. O.; Oyefolu, P. K.; Kusuma, H. S. A Comprehensive Review of Recent Advances in the Synthesis and Application of Metal-Organic Frameworks (MOFs) for the Adsorptive Sequestration of Pollutants from Wastewater. *Sep. Purif. Technol.* **2023**, *311*, 123246.
(18) Sharanyakanth, P. S.; Radhakrishnan, M. Synthesis of Metal-Organic Frameworks (MOFs) and Its Application in Food Packaging: A Critical Review. *Trends Food Sci. Technol.* **2020**, *104*, 102−116.
(19) Annamalai, J.; Murugan, P.; Ganapathy, D.; Nallaswamy, D.; Atchudan, R.; Arya, S.; Khosla, A.; Barathi, S.; Sundramoorthy, A. K. Synthesis of Various Dimensional Metal Organic Frameworks (MOFs) and Their Hybrid Composites for Emerging Applications − A Review. *Chemosphere* **2022**, *298*, 134184.
(20) Stassen, I.; Burtch, N.; Talin, A.; Falcaro, P.; Allendorf, M.; Ameloot, R. An Updated Roadmap for the Integration of Metal−Organic Frameworks with Electronic Devices and Chemical Sensors. *Chem. Soc. Rev.* **2017**, *46* (11), 3185−3241.
(21) Xiao, Y.-H.; Gu, Z.-G.; Zhang, J. Surface-Coordinated Metal−Organic Framework Thin Films (SURMOFs) for Electrocatalytic Applications. *Nanoscale* **2020**, *12* (24), 12712−12730.
(22) Chen, D.-H.; Gliemann, H.; Wöll, C. Layer-by-Layer Assembly of Metal-Organic Framework Thin Films: Fabrication and Advanced Applications. *Chem. Phys. Rev.* **2023**, *4* (1), 011305.
(23) Stock, N.; Biswas, S. Synthesis of Metal-Organic Frameworks (MOFs): Routes to Various MOF Topologies, Morphologies, and Composites. *Chem. Rev.* **2012**, *112* (2), 933−969.
(24) Shi, X.; Shan, Y.; Du, M.; Pang, H. Synthesis and Application of Metal-Organic Framework Films. *Coord. Chem. Rev.* **2021**, *444*, 214060.
(25) Falcaro, P.; Okada, K.; Hara, T.; Ikigaki, K.; Tokudome, Y.; Thornton, A. W.; Hill, A. J.; Williams, T.; Doonan, C.; Takahashi, M. Centimetre-Scale Micropore Alignment in Oriented Polycrystalline Metal−Organic Framework Films via Heteroepitaxial Growth. *Nat. Mater.* **2017**, *16* (3), 342−348.
(26) Okada, K.; Nakanishi, M.; Ikigaki, K.; Tokudome, Y.; Falcaro, P.; Doonan, C. J.; Takahashi, M. Controlling the Alignment of 1D Nanochannel Arrays in Oriented Metal−Organic Framework Films for Host−Guest Materials Design. *Chem. Sci.* **2020**, *11* (30), 8005−8012.
(27) Ikigaki, K.; Okada, K.; Tokudome, Y.; Toyao, T.; Falcaro, P.; Doonan, C. J.; Takahashi, M. MOF-on-MOF: Oriented Growth of Multiple Layered Thin Films of Metal−Organic Frameworks. *Angew. Chem.* **2019**, *131* (21), 6960−6964.
(28) Zojer, E.; Winkler, C. Maximizing the Carrier Mobilities of Metal−Organic Frameworks Comprising Stacked Pentacene Units. *J. Phys. Chem. Lett.* **2021**, *12* (29), 7002−7009.
(29) Xie, L. S.; Skorupskii, G.; Dincă, M. Electrically Conductive Metal−Organic Frameworks. *Chem. Rev.* **2020**, *120* (16), 8536−8580.
(30) Linares-Moreau, M.; Brandner, L. A.; Velásquez-Hernández, M. d. J.; Fonseca, J.; Benseghir, Y.; Chin, J. M.; Maspoch, D.; Doonan, C.; Falcaro, P. Fabrication of Oriented Polycrystalline MOF Superstructures. *Adv. Mater.* **2024**, *36* (1), 2309645.
(31) Choe, M.; Koo, J. Y.; Park, I.; Ohtsu, H.; Shim, J. H.; Choi, H. C.; Park, S. S. Chemical Vapor Deposition of Edge-on Oriented 2D Conductive Metal−Organic Framework Thin Films. *J. Am. Chem. Soc.* **2022**, *144* (37), 16726−16731.
(32) Han, S.; Mullins, C. B. Current Progress and Future Directions in Gas-Phase Metal-Organic Framework Thin-Film Growth. *ChemSusChem* **2020**, *13* (20), 5433−5442.
(33) Birkholz, M. *Thin Film Analysis by X-Ray Scattering*; John Wiley & Sons, 2006.
(34) Werzer, O.; Kowarik, S.; Gasser, F.; Jiang, Z.; Strzalka, J.; Nicklin, C.; Resel, R. X-Ray Diffraction under Grazing Incidence Conditions. *Nat. Rev. Methods Primers* **2024**, *4*, 15.
(35) Fumagalli, E.; Campione, M.; Raimondo, L.; Sassella, A.; Moret, M.; Barba, L.; Arrighetti, G. Grazing-Incidence X-Ray Diffraction Study of Rubrene Epitaxial Thin Films. *J. Synchrotron Radiat.* **2012**, *19* (5), 682−687.
(36) Steele, J. A.; Solano, E.; Hardy, D.; Dayton, D.; Ladd, D.; White, K.; Chen, P.; Hou, J.; Huang, H.; Saha, R. A.; Wang, L.; Gao, F.; Hofkens, J.; Roeffaers, M. B. J.; Chernyshov, D.; Toney, M. F. How to GIWAXS: Grazing Incidence Wide Angle X-Ray Scattering Applied to Metal Halide Perovskite Thin Films. *Adv. Energy Mater.* **2023**, *13* (27), 2300760.
(37) Multia, J.; Kravchenko, D. E.; Rubio-Giménez, V.; Philip, A.; Ameloot, R.; Karppinen, M. Nanoporous Metal−Organic Framework Thin Films Prepared Directly from Gaseous Precursors by Atomic and Molecular Layer Deposition: Implications for Microelectronics. *ACS Appl. Nano Mater.* **2023**, *6* (2), 827−831.
(38) Legenstein, L.; Rodríguez-Hermida, S.; Rubio-Giménez, V.; Stassin, T.; Hofer, S.; Kainz, M. P.; Fratschko, M.; Carraro, F.; Falcaro, P.; Ameloot, R.; Resel, R. Identifying the Internal Network Structure of a New Copper Isonicotinate Thin-Film Polymorph Obtained via Chemical Vapor Deposition. *Adv. Mater. Interfaces* **2023**, *10* (12), 2202461.
(39) Schrode, B.; Pachmajer, S.; Dohr, M.; Röthel, C.; Domke, J.; Fritz, T.; Resel, R.; Werzer, O. GIDVis A Comprehensive Software Tool for Geometry-Independent Grazing-Incidence X-Ray Diffraction Data Analysis and Pole-Figure Calculations. *J. Appl. Crystallogr.* **2019**, *52* (3), 683−689.
(40) Ranjan, R.; Tsapatsis, M. Microporous Metal Organic Framework Membrane on Porous Support Using the Seeded Growth Method. *Chem. Mater.* **2009**, *21* (20), 4920−4924.
(41) Rubio-Giménez, V.; Carraro, F.; Hofer, S.; Fratschko, M.; Stassin, T.; Rodríguez-Hermida, S.; Schrode, B.; Barba, L.; Resel, R.; Falcaro, P.; Ameloot, R. Polymorphism and Orientation Control of Copper-Dicarboxylate Metal−Organic Framework Thin Films through Vapour- and Liquid-Phase Growth. *CrystEngComm* **2024**, *26* (8), 1071−1076.
(42) Henke, S.; Schneemann, A.; Wütscher, A.; Fischer, R. A. Directing the Breathing Behavior of Pillared-Layered Metal−Organic Frameworks via a Systematic Library of Functionalized Linkers Bearing Flexible Substituents. *J. Am. Chem. Soc.* **2012**, *134* (22), 9464−9474.
(43) Seki, K.; Takamizawa, S.; Mori, W. Design and Gas Adsorption Property of a Three-Dimensional Coordination Polymer with a Stable and Highly Porous Framwork. *Chem. Lett.* **2001**, *30* (4), 332−333.
(44) Tourani, H.; Naimi-Jamal, M. R.; Panahi, L.; Dekamin, M. G. Nanoporous Metal-Organic Framework Cu2(BDC)2(DABCO) as an Efficient Heterogeneous Catalyst for One-Pot Facile Synthesis of 1,2,3-Triazole Derivatives in Ethanol: Evaluating Antimicrobial Activity of the Novel Derivatives. *Sci. Iran.* **2019**, *26* (3), 1485−1496.
(45) Seki, K.; Mori, W. Syntheses and Characterization of Microporous Coordination Polymers with Open Frameworks. *J. Phys. Chem. B* **2002**, *106* (6), 1380−1385.
(46) Maes, M.; Schouteden, S.; Hirai, K.; Furukawa, S.; Kitagawa, S.; De Vos, D. E. Liquid Phase Separation of Polyaromatics on [$Cu_2(BDC)_2(Dabco)$]. *Langmuir* **2011**, *27* (15), 9083−9087.
(47) Takei, T.; Kawashima, J.; Ii, T.; Maeda, A.; Hasegawa, M.; Kitagawa, T.; Ohmura, T.; Ichikawa, M.; Hosoe, M.; Kanoya, I.; Mori, W. Hydrogen Adsorption Properties of Lantern-Type Dinuclear M(BDC)(DABCO)1/2. *BCSJ.* **2008**, *81* (7), 847−856.
(48) Shekhah, O.; Wang, H.; Kowarik, S.; Schreiber, F.; Paulus, M.; Tolan, M.; Sternemann, C.; Evers, F.; Zacher, D.; Fischer, R. A.; Wöll,


https://doi.org/10.1021/acs.cgd.4c01433
*Cryst. Growth Des.* 2025, 25, 3665−3679

C. Step-by-Step Route for the Synthesis of Metal−Organic Frameworks. *J. Am. Chem. Soc.* **2007**, *129* (49), 15118−15119.
(49) Fischer, J. C.; Li, C.; Hamer, S.; Heinke, L.; Herges, R.; Richards, B. S.; Howard, I. A. GIWAXS Characterization of Metal−Organic Framework Thin Films and Heterostructures: Quantifying Structure and Orientation. *Adv. Mater. Interfaces* **2023**, *10* (11), 2202259.
(50) McCarthy, B. D.; Liseev, T.; Beiler, A. M.; Materna, K. L.; Ott, S. Facile Orientational Control of M2L2P SURMOFs on ⟨100⟩ Silicon Substrates and Growth Mechanism Insights for Defective MOFs. *ACS Appl. Mater. Interfaces* **2019**, *11* (41), 38294−38302.
(51) Velásquez-Hernández, M. d. J.; Linares-Moreau, M.; Brandner, L. A.; Marmiroli, B.; Barella, M.; Acuna, G. P.; Zilio, S. D.; Verstreken, M. F. K.; Kravchenko, D. E.; Linder-Patton, O. M.; Evans, J. D.; Wiltsche, H.; Carraro, F.; Wolinski, H.; Ameloot, R.; Doonan, C.; Falcaro, P. Fabrication of 3D Oriented MOF Micropatterns with Anisotropic Fluorescent Properties. *Adv. Mater.* **2023**, *35* (25), 2211478.
(52) Linares-Moreau, M.; Brandner, L. A.; Kamencek, T.; Klokic, S.; Carraro, F.; Okada, K.; Takahashi, M.; Zojer, E.; Doonan, C. J.; Falcaro, P. Semi-Automatic Deposition of Oriented Cu(OH)2 Nanobelts for the Heteroepitaxial Growth of Metal−Organic Framework Films. *Adv. Mater. Interfaces* **2021**, *8* (21), 2101039.
(53) Seo, S.-D.; Jin, Y.-H.; Lee, S.-H.; Shim, H.-W.; Kim, D.-W. Low-Temperature Synthesis of CuO-Interlaced Nanodiscs for Lithium Ion Battery Electrodes. *Nanoscale Res. Lett.* **2011**, *6* (1), 397.
(54) *Base Package*. https://www.bruker.com/en/products-and-solutions/infrared-and-raman/opus-spectroscopy-software/base-package.html (accessed 2023−09−20).
(55) *OriginPro | Datenanalyse- und Grafiksoftware*. https://www.additive-net.de/en/software/produkte/originlab/originpro (accessed 2024−07−03).
(56) Gasser, F.; Simbrunner, J.; Steinrück, H.-G.; Resel, R. Intensity Corrections for Grazing Incidence X-Ray Diffraction Using Static Area Detectors. *J. Appl. Crystallogr.* **2025**, *58*, 96.
(57) Schulz, L. G. A Direct Method of Determining Preferred Orientation of a Flat Reflection Sample Using a Geiger Counter X-Ray Spectrometer. *J. Appl. Phys.* **1949**, *20* (11), 1030.
(58) Resel, R.; Lengyel, O.; Haber, T.; Werzer, O.; Hardeman, W.; de Leeuw, D. M.; Wondergem, H. J. Wide-Range Three-Dimensional Reciprocal-Space Mapping: A Novel Approach Applied to Organic Monodomain Thin Films. *J. Appl. Crystallogr.* **2007**, *40* (3), 580−582.
(59) Salzmann, I.; Resel, R. S. T. E. R. E. O. P. O. L. E. *STEREOPOLE*: software for the analysis of X-ray diffraction pole figures with IDL. *J. Appl. Crystallogr.* **2004**, *37* (6), 1029−1033.
(60) Heffelfinger, C. J.; Burton, R. L. X-Ray Determination of the Crystallite Orientation Distributions of Polyethylene Terephthalate Films. *J. Polym. Sci.* **1960**, *47* (149), 289−306.
(61) Blum, V.; Gehrke, R.; Hanke, F.; Havu, P.; Havu, V.; Ren, X.; Reuter, K.; Scheffler, M. Ab Initio Molecular Simulations with Numeric Atom-Centered Orbitals. *Comput. Phys. Commun.* **2009**, *180* (11), 2175−2196.
(62) Kresse, G.; Furthmüller, J. Efficiency of Ab-Initio Total Energy Calculations for Metals and Semiconductors Using a Plane-Wave Basis Set. *Comput. Mater. Sci.* **1996**, *6* (1), 15−50.
(63) Kresse, G.; Joubert, D. From Ultrasoft Pseudopotentials to the Projector Augmented-Wave Method. *Phys. Rev. B* **1999**, *59* (3), 1758−1775.
(64) Kim, Y.; Haldar, R.; Kim, H.; Koo, J.; Kim, K. The Guest-Dependent Thermal Response of the Flexible MOF Zn 2 (BDC) 2 (DABCO). *Dalton Trans.* **2016**, *45* (10), 4187−4192.
(65) Tkatchenko, A.; DiStasio, R. A.; Car, R.; Scheffler, M. Accurate and Efficient Method for Many-Body van Der Waals Interactions. *Phys. Rev. Lett.* **2012**, *108* (23), 236402.
(66) Ambrosetti, A.; Reilly, A. M.; DiStasio, R. A., Jr.; Tkatchenko, A. Long-Range Correlation Energy Calculated from Coupled Atomic Response Functions. *J. Chem. Phys.* **2014**, *140* (18), 18A508.
(67) Grimme, S.; Antony, J.; Ehrlich, S.; Krieg, H. A Consistent and Accurate Ab Initio Parametrization of Density Functional Dispersion Correction (DFT-D) for the 94 Elements H-Pu. *J. Chem. Phys.* **2010**, *132* (15), 154104.
(68) *VASP. KPIONT*. https://www.vasp.at/wiki/index.php/KPOINTS (accessed 2024−06−28).
(69) Strasser, N.; Wieser, S.; Zojer, E. Predicting Spin-Dependent Phonon Band Structures of HKUST-1 Using Density Functional Theory and Machine-Learned Interatomic Potentials. *Int. J. Mol. Sci.* **2024**, *25* (5), 3023.
(70) *VASP. IBRION*. https://www.vasp.at/wiki/index.php/IBRION (accessed 2024−07−02).
(71) Togo, A.; Tanaka, I. First Principles Phonon Calculations in Materials Science. *Scr. Mater.* **2015**, *108*, 1−5.
(72) Baroni, S.; De Gironcoli, S.; Dal Corso, A.; Giannozzi, P. Phonons and Related Crystal Properties from Density-Functional Perturbation Theory. *Rev. Mod. Phys.* **2001**, *73* (2), 515.
(73) Bedoya-Martínez, N.; Giunchi, A.; Salzillo, T.; Venuti, E.; Della Valle, R. G.; Zojer, E. Toward a Reliable Description of the Lattice Vibrations in Organic Molecular Crystals: The Impact of van Der Waals Interactions. *J. Chem. Theory Comput.* **2018**, *14* (8), 4380−4390.
(74) Bedoya-Martínez, N.; Schrode, B.; Jones, A. O.; Salzillo, T.; Ruzié, C.; Demitri, N.; Geerts, Y. H.; Venuti, E.; Della Valle, R. G.; Zojer, E.; et al. DFT-Assisted Polymorph Identification from Lattice Raman Fingerprinting. *J. Phys. Chem. Lett.* **2017**, *8* (15), 3690−3695.
(75) Donà, L.; Brandenburg, J. G.; Civalleri, B. Metal−Organic Frameworks Properties from Hybrid Density Functional Approximations. *J. Chem. Phys.* **2022**, *156* (9), 094706.
(76) Zvereva, E. E.; Shagidullin, A. R.; Katsyuba, S. A. Ab Initio and DFT Predictions of Infrared Intensities and Raman Activities. *J. Phys. Chem. A* **2011**, *115* (1), 63−69.
(77) Katsyuba, S. A.; Zvereva, E. E.; Burganov, T. I. Is There a Simple Way to Reliable Simulations of Infrared Spectra of Organic Compounds? *J. Phys. Chem. A* **2013**, *117* (30), 6664−6670.
(78) Palotás, J.; Martens, J.; Berden, G.; Oomens, J. The Infrared Spectrum of Protonated Buckminsterfullerene C60H+. *Nat. Astron* **2020**, *4* (3), 240−245.
(79) Aleksandrov, H. A.; Zdravkova, V. R.; Mihaylov, M. Y.; Petkov, P. St.; Vayssilov, G. N.; Hadjiivanov, K. I. Precise Identification of the Infrared Bands of the Polycarbonyl Complexes on Ni−MOR Zeolite by $^{12}$ C $^{16}$ O− $^{13}$ C $^{18}$ O Coadsorption and Computational Modeling. *J. Phys. Chem. C* **2012**, *116* (43), 22823−22831.
(80) Erba, A.; Desmarais, J. K.; Casassa, S.; Civalleri, B.; Donà, L.; Bush, I. J.; Searle, B.; Maschio, L.; Edith-Daga, L.; Cossard, A.; Ribaldone, C.; Ascrizzi, E.; Marana, N. L.; Flament, J.-P.; Kirtman, B. CRYSTAL23: A Program for Computational Solid State Physics and Chemistry. *J. Chem. Theory Comput.* **2023**, *19*, 6891.
(81) Becke, A. D. Density-Functional Thermochemistry. III. The Role of Exact Exchange. *J. Chem. Phys.* **1993**, *98* (7), 5648−5652.
(82) Lee, C.; Yang, W.; Parr, R. G. Development of the Colle-Salvetti Correlation-Energy Formula into a Functional of the Electron Density. *Phys. Rev. B* **1988**, *37* (2), 785−789.
(83) Grimme, S.; Ehrlich, S.; Goerigk, L. Effect of the Damping Function in Dispersion Corrected Density Functional Theory. *J. Comput. Chem.* **2011**, *32* (7), 1456−1465.
(84) Schäfer, A.; Horn, H.; Ahlrichs, R. Fully Optimized Contracted Gaussian Basis Sets for Atoms Li to Kr. *J. Chem. Phys.* **1992**, *97* (4), 2571−2577.
(85) Vilela Oliveira, D.; Laun, J.; Peintinger, M. F.; Bredow, T. BSSE-Correction Scheme for Consistent Gaussian Basis Sets of Double- and Triple-Zeta Valence with Polarization Quality for Solid-State Calculations. *J. Comput. Chem.* **2019**, *40* (27), 2364−2376.
(86) Pascale, F.; Tosoni, S.; Zicovich-Wilson, C.; Ugliengo, P.; Orlando, R.; Dovesi, R. Vibrational Spectrum of Brucite, Mg(OH)2: A Periodic Ab Initio Quantum Mechanical Calculation Including OH Anharmonicity. *Chem. Phys. Lett.* **2004**, *396* (4−6), 308−315.
(87) Lindberg, B. A New Efficient Method for Calculation of Energy Eigenvalues and Eigenstates of the One-Dimensional Schrödinger Equation. *J. Chem. Phys.* **1988**, *88* (6), 3805−3810.
(88) Chen, Z.; Xiang, S.; Zhao, D.; Chen, B. Reversible Two-Dimensional−Three Dimensional Framework Transformation within a


https://doi.org/10.1021/acs.cgd.4c01433
Cryst. Growth Des. 2025, 25, 3665−3679

Prototype Metal−Organic Framework. *Cryst. Growth Des.* **2009**, *9* (12), 5293−5296.
(89) Giacovazzo, C. Isomorphous Replacement Techniques. In *Phasing in Crystallography: A Modern Perspective*; Giacovazzo, C., Ed.; Oxford University Press, 2013 .
(90) Tiana, D.; Hendon, C. H.; Walsh, A. Ligand Design for Long-Range Magnetic Order in Metal−Organic Frameworks. *Chem. Commun.* **2014**, *50* (90), 13990−13993.
(91) Pöppl, A.; Kunz, S.; Himsl, D.; Hartmann, M. C. W. and Pulsed ESR Spectroscopy of Cupric Ions in the Metal− Organic Framework Compound Cu3 (BTC) 2. *J. Phys. Chem. C* **2008**, *112* (7), 2678−2684.
(92) Zhang, X. X.; Chui, S. S.-Y.; Williams, I. D. Cooperative Magnetic Behavior in the Coordination Polymers [Cu3 (TMA) 2L3](L= H2O, Pyridine). *J. Appl. Phys.* **2000**, *87* (9), 6007−6009.
(93) Baumgartner, B.; Ikigaki, K.; Okada, K.; Takahashi, M. Infrared Crystallography for Framework and Linker Orientation in Metal−Organic Framework Films. *Chem. Sci.* **2021**, *12* (27), 9298−9308.
(94) von Jaggi, H.; Oswald, H. R. Die Kristallstruktur Des Kupferhydroxids Cu(OH)2. *Acta Crystallogr.* **1961**, *14* (10), 1041−1045.
(95) Oswald, H. R.; Reller, A.; Schmalle, H. W.; Dubler, E. Structure of Copper(II) Hydroxide, Cu(OH)2. *Acta Cryst. C* **1990**, *46* (12), 2279−2284.
(96) Brandner, L. A.; Linares-Moreau, M.; Zhou, G.; Amenitsch, H.; Dal Zilio, S.; Huang, Z.; Doonan, C.; Falcaro, P. Water Sensitivity of Heteroepitaxial Cu-MOF Films: Dissolution and Re-Crystallization of 3D-Oriented MOF Superstructures. *Chem. Sci.* **2023**, *14* (43), 12056−12067.
(97) Fischer, J. C.; Steentjes, R.; Chen, D.-H.; Richards, B. S.; Zojer, E.; Wöll, C.; Howard, I. A. Determining Structures of Layer-by-Layer Spin-Coated Zinc Dicarboxylate-Based Metal-Organic Thin Films. *Chem.—Eur. J.* **2024**, *30* (37), No. e202400565.
(98) Klug, H. P.; Alexander, L. E. *X-Ray Diffraction Procedures: For Polycrystalline and Amorphous Materials*, 2nd ed., 1974.
(99) Heinke, L.; Tu, M.; Wannapaiboon, S.; Fischer, R. A.; Wöll, C. Surface-Mounted Metal-Organic Frameworks for Applications in Sensing and Separation. *Microporous Mesoporous Mater.* **2015**, *216*, 200−215.
(100) Kidd, P. *XRD of Gallium Nitride and Related Compounds: Strain, Composition and Layer Thickness*; Panalytical: Almelo: Netherlands, 2009.
(101) Forker, R.; Meissner, M.; Fritz, T. Classification of Epitaxy in Reciprocal and Real Space: Rigid versus Flexible Lattices. *Soft Matter* **2017**, *13* (9), 1748−1758.
(102) Tarzia, A.; Takahashi, M.; Falcaro, P.; Thornton, A. W.; Doonan, C. J.; Huang, D. M. High-Throughput Screening of Metal−Organic Frameworks for Macroscale Heteroepitaxial Alignment. *ACS Appl. Mater. Interfaces* **2018**, *10* (47), 40938−40950.
(103) Koseki, Y.; Okada, K.; Hashimoto, S.; Hirouchi, S.; Fukatsu, A.; Takahashi, M. Improved Optical Quality of Heteroepitaxially Grown Metal−Organic Framework Thin Films by Modulating the Crystal Growth. *Nanoscale* **2024**, *16* (29), 14101−14107.
(104) Jhariat, P.; Kareem, A.; Kumari, P.; Sarfudeen, S.; Panda, P.; Senthilkumar, S.; Panda, T. A Series of Isostructural Metal−Organic Frameworks for an Enhanced Electro-Catalytic Oxygen Evolution Reaction. *Dalton Trans.* **2024**, *53* (15), 6568−6574.
(105) Zhang, M.; Lin, Q.; Wu, W.; Ye, Y.; Yao, Z.; Ma, X.; Xiang, S.; Zhang, Z. Isostructural MOFs with Higher Proton Conductivity for Improved Oxygen Evolution Reaction Performance. *ACS Appl. Mater. Interfaces* **2020**, *12* (14), 16367−16375.
(106) Sammawipawekul, N.; Kaeosamut, N.; Autthawong, T.; Watwiangkham, A.; Suthirakun, S.; Wannapaiboon, S.; Mahamai, N.; Sarakonsri, T.; Chimupala, Y.; Yimklan, S. Isostructural Dual-Ligand-Based MOFs with Different Metal Centers in Response to Diverse Capacity Lithium-Ion Battery Anode. *Chem. Eng. J.* **2024**, *482*, 148904.
(107) Kintzel, E. J., Jr.; Smilgies, D.-M.; Skofronick, J. G.; Safron, S. A.; Van Winkle, D. H.; Trelenberg, T. W.; Akhadov, E. A.; Flaherty, F. A. Investigation of the Morphology of the Initial Growth of the Aromatic Molecule P-Quaterphenyl on NaCl (001). *J. Vac. Sci. Technol., A* **2001**, *19* (4), 1270−1276.
(108) Hoffman, J. M.; Thompson, N. B.; Borkiewicz, O.; He, X.; Amsterdam, S.; Xie, Z.; Taggart, A.; Mulfort, K. L.; Martinson, A. B. F.; Chen, L. X.; Ruett, U.; Tiede, D. M. Orientational Analysis of Atomic Pair Correlations in Nanocrystalline Indium Oxide Thin Films. *IUCrJ.* **2024**, *11* (1), 120−128.
(109) Werzer, O.; Matoy, K.; Smilgies, D.-M.; Rothmann, M. M.; Strohriegl, P.; Resel, R. Uniaxially Aligned Poly[(9,9-Dioctylfluorenyl-2,7-Diyl)-Co-Bithiophene] Thin Films Characterized by the X-Ray Diffraction Pole Figure Technique. *J. Appl. Polym. Sci.* **2008**, *107* (3), 1817−1821.
(110) Röthel, C.; Ehmann, H. M. A.; Baumgartner, R.; Reischl, D.; Werzer, O. Alteration of Texture and Polymorph of Phenytoin within Thin Films and Its Impact on Dissolution. *CrystEngComm* **2016**, *18* (4), 588−595.
(111) Alexander, L. E. *X-Ray Diffraction Methods in Polymer Science*; Wiley-Interscience, 1969.
(112) de Poel, W.; Pintea, S.; Drnec, J.; Carla, F.; Felici, R.; Mulder, P.; Elemans, J. A. A. W.; van Enckevort, W. J. P.; Rowan, A. E.; Vlieg, E. Muscovite Mica: Flatter than a Pancake. *Surf. Sci.* **2014**, *619*, 19−24.
(113) Simbrunner, J.; Salzmann, I.; Resel, R. Indexing of Grazing-Incidence X-Ray Diffraction Patterns. *Crystallogr. Rev.* **2023**, *29*, 19−37.
(114) Wang, Z.; Liu, J.; Lukose, B.; Gu, Z.; Weidler, P. G.; Gliemann, H.; Heine, T.; Wöll, C. Nanoporous Designer Solids with Huge Lattice Constant Gradients: Multiheteroepitaxy of Metal−Organic Frameworks. *Nano Lett.* **2014**, *14* (3), 1526−1529.
(115) PambudiAndersonAttfield, F. I. M. W. M. P. W.; Anderson, M.; Attfield, P. Unveiling the mechanism of lattice-mismatched crystal growth of a core−shell metal−organic framework. *Chem. Sci.* **2019**, *10* (41), 9571−9575.
(116) Nascimbeni, G.; Wöll, C.; Zojer, E. Electrostatic Design of Polar Metal−Organic Framework Thin Films. *Nanomaterials* **2020**, *10* (12), 2420.
(117) Nefedov, A.; Haldar, R.; Xu, Z.; Kühner, H.; Hofmann, D.; Goll, D.; Sapotta, B.; Hecht, S.; Krstić, M.; Rockstuhl, C.; Wenzel, W.; Bräse, S.; Tegeder, P.; Zojer, E.; Wöll, C. Avoiding the Center-Symmetry Trap: Programmed Assembly of Dipolar Precursors into Porous, Crystalline Molecular Thin Films. *Adv. Mater.* **2021**, *33* (35), 2103287.
(118) Wang, H.; Vagin, S. I.; Lane, S.; Lin, W.; Shyta, V.; Heinz, W. R.; Van Dyck, C.; Bergren, A. J.; Gardner, K.; Rieger, B.; Meldrum, A. Metal−Organic Framework with Color-Switching and Strongly Polarized Emission. *Chem. Mater.* **2019**, *31* (15), 5816−5823.
(119) Zhang, J.-R.; Zhang, H.-Y.; Guo, J.-H.; Liu, Z.-H.; Ma, C.-Y.; Yang, X.-G.; Lu, X.-Y.; Qin, J.-H.; Ma, L.-F. An Anthracene Based Metal−Organic Framework Showing Efficient Angle-Dependent Polarized Emission, Luminescence Thermometry, and Photoelectronic Response. *Dalton Trans.* **2022**, *51* (5), 1769−1774.


https://doi.org/10.1021/acs.cgd.4c01433
*Cryst. Growth Des.* 2025, 25, 3665−3679